

Shape Optimization for Thermoacoustic Instability of Combustors



Ekrem Ekici

Supervisor: Prof. Matthew P. Juniper

Advisor: Prof. Stewart Cant

Department of Engineering
University of Cambridge

This dissertation is submitted for the
First Year Report

Declaration

I hereby declare that except where specific reference is made to the work of others, the contents of this dissertation are original and have not been submitted in whole or in part for consideration for any other degree or qualification in this, or any other university. This dissertation is my own work and contains nothing which is the outcome of work done in collaboration with others, except as specified in the text. This dissertation contains fewer than 65,000 words including appendices, bibliography, footnotes, tables and equations and has fewer than 150 figures.

Ekrem Ekici
November 2021

Abstract

Thermoacoustic instability is a major threat for combustion systems. The catastrophic consequences might occur such as oscillations in thrust, structural damage or eventually engine failure. Thermoacoustic instabilities are generally recur in the later stages of development process. Since numerous parameters should be tuned elegantly due to the extreme sensitivity of thermoacoustic systems, numerical tools are becoming practical to stabilize the system. By adjoint methods, the computation of gradient informations for system parameters becomes relatively cheap compared to other methods such as finite difference methods.

In this report, shape sensitivity of eigenvalues of a thermoacoustic system is presented. Possible changes in the shape of the geometries are discussed to reduce thermoacoustic instability. To start, Helmholtz equation with unsteady heat release rate term is derived and discretized with finite element method. Helmholtz solver is coupled with adjoint based shape optimization method. As a case study, canonical thermoacoustic system, Rijke tube is investigated using Dolfin and Dolfinx. Eigenmodes are determined for 1D and 2D configurations. Then, 2D domain is stabilized thermoacoustically by making minor changes on boundaries. Additionally, solver's capability on calculating eigenmodes and shape derivatives for 3D combustors is also presented. Azimuthal degenerate modes of different geometries of MICCA combustor and realistic combustor have been successfully captured by implemented solver. By using adjoint method, the shape derivative information is obtained cheaply for each combustor geometry.

Table of contents

List of figures	ix
List of tables	xi
Nomenclature	xiii
1 Introduction	1
1.1 Background	1
1.2 Thermoacoustic Mechanism	1
1.3 Analyzing Thermoacoustic Instabilities	2
1.3.1 Large Eddy Simulations	2
1.3.2 Helmholtz solvers	3
1.4 Thermoacoustic Modes	3
1.5 Control Methods	4
1.5.1 Feedback Control (Closed Loop Control)	4
1.5.2 Passive Control Methods	5
1.6 Motivation of the study	5
2 Mathematical Model of Thermoacoustic Instability	7
2.1 Thermoacoustic Helmholtz Equation	7
2.2 Source Term in Helmholtz Equation	11
2.3 Flame Transfer Function (FTF)	11
2.4 Boundary Conditions for Helmholtz Equation	12
3 Finite Element Based Helmholtz Solver	13
3.1 Finite Element Method Definitions	14
3.2 Passive Flame Discretization	14
3.3 Active Flame Discretization	16
3.4 Solution of Quadratic Eigenvalue Problem	17

3.5	Implemented Helmholtz Solver	18
4	Sensitivity of the Eigenvalue with Adjoint	21
4.1	Left Eigenvector	21
4.2	Base State Sensitivities	22
4.3	Shape State Sensitivities	24
4.3.1	Basic Shape Calculus	24
4.3.2	Shape Derivative for Boundary Condition	25
4.3.3	Shape Derivatives for Eigenvalue	27
4.4	Taylor Remainder Test	29
5	Results	31
5.1	Rijke Tube	31
5.1.1	Eigenmodes	32
5.1.2	Base State Sensitivities	35
5.1.3	Shape Optimization	35
5.2	MICCA Combustor	39
5.2.1	Micca - Base Case	40
5.2.2	Micca - Extended Plenum	44
5.2.3	Micca - Extended Plenum with Cooling Holes	47
5.3	Realistic Combustor	50
6	Further Work	55
6.1	Current Findings	55
6.2	Future Work	55
	References	59
	Appendix A Thermoacoustic Eigensolver	63
	Appendix B Nondimensionalization	65
	Appendix C BSpline Curves	67
C.1	Simple Example	67

List of figures

3.1	Proposed Methodology	19
5.1	Eigenmodes of Rijke Tube in Dolfin Code [28]	33
5.2	Eigenmodes of Rijke Tube in Dolfinx Code	34
5.4	Shape Derivatives (ω') of each control point for Rijke Tube in Dolfin [17]	36
5.5	Shape Derivatives (ω') of each control point for Rijke Tube in Dolfinx	37
5.6	Optimized geometry of Rijke Tube [17]	38
5.7	Geometry of Micca Combustor	40
5.8	Eigenmodes of Micca Combustor	41
5.9	Phase shift between P_1 and P_2	42
5.10	Shape derivatives for MICCA - base case	43
5.11	Geometry of Micca Combustor - extended plenum case	44
5.12	Eigenmodes of Micca Combustor - extended plenum case	45
5.13	Shape derivatives for MICCA - extended plenum case	46
5.14	Geometry of Micca Combustor with cooling holes	47
5.15	Eigenmodes of Micca Combustor - extended plenum with cooling holes	48
5.16	Shape derivatives for MICCA - extended plenum with cooling holes	49
5.17	Real combustor geometry and mesh	50
5.18	Eigenmodes of realistic combustor	51
5.19	Shape derivatives for realistic combustor	53
6.1	Proposed Gantt Chart	57
C.1	Basis functions for BSpline curve	68
C.2	BSpline curve and its xy points	68

List of tables

- 5.1 Dimensional and non-dimensional parameters of modelled Rijke Tube [7] 32
- 5.2 Dimensional parameters of Micca combustor 39

- B.1 Nondimensionalization of Quantities 65
- B.2 Nondimensionalization of parameter n 65

Nomenclature

Greek Symbols

c	speed of sound
c_p	specific heat capacity at constant pressure
c_v	specific heat capacity at constant volume
γ	heat capacity ratio
Γ	reflection coefficient
i	unit imaginary number $\sqrt{-1}$
\mathbf{n}	unit normal vector
ω	angular frequency
p	pressure
Q	volumetric heat release rate
q	heat release rate
R	universal gas constant
ρ	density
s	entropy
T	temperature
t	time
u	velocity

\mathbf{u}	velocity vector
U_b	bulk velocity
\mathbf{x}	position vector
Z	specific acoustic impedance

Superscripts

*	complex conjugate
---	-------------------

Subscripts

0	mean quantity
1	perturbed quantity
a	ambient
d	downstream
r	reference point
u	upstream

Other Symbols

\Im	imaginary part of complex number
\mathcal{L}	linear differential operator
∇	gradient operator
\Re	real part of complex number

Acronyms / Abbreviations

CFD	Computational Fluid Dynamics
FEM	Finite Element Method
FTF	Flame Transfer Function
LES	Large Eddy Simulation

Chapter 1

Introduction

1.1 Background

Thermoacoustic instability is a major problem which threatens the sustainable operability of gas turbine engines. Growing oscillations in the combustor chamber might lead to detrimental vibrations that increase the fatigue of engine components. High amplitude acoustic oscillations can extinguish the flame. For these reasons, it would be useful to be able to predict thermoacoustic behaviour during the development process of aero-engines. Nowadays, developing computational power allows the problem to be analysed more quickly. In this way, Helmholtz solvers can give results in sufficiently short times that they could enable optimization of the system thermoacoustically. Additionally, experimental studies are used to generate flame transfer functions which are essential for Helmholtz solvers.

This introduction section follows the following structure; Firstly, thermoacoustic mechanism and analysing techniques for thermoacoustic instabilities are presented. After that, thermoacoustic modes and control techniques for instabilities are summarized. Lastly, motivation of the study is proposed.

1.2 Thermoacoustic Mechanism

Thermoacoustic oscillation mechanism can be explained by means of an analogy between flame-acoustic waves and classical piston engine in internal combustion engines [1]; piston replaces with acoustic waves and flame replaces with ignited gas in the combustor. When the acoustic waves meet the flame, the flame gets perturbed due to sound waves and its shape is inevitably changes in which lead to unsteady heat release rate. Then heat is converted into work on acoustic waves and if this work is not dissipated in the chamber, then

acoustic oscillations start to grow. Eventually, system is starting to behave thermoacoustically unstable.

$$\int_V \frac{(\gamma - 1) \overline{p'q}}{\overline{\rho c^2}} dV > \int_S \overline{p' \mathbf{u}} \cdot d\mathbf{S} \quad (1.1)$$

where overline denotes an average quantity over one period of thermoacoustic oscillation, p' is acoustic pressure, q is heat release rate and \mathbf{u} is particle velocity, γ is ratio of specific heat capacities, c is speed of sound and ρ is density. Equation (1.1) is called general form of Rayleigh's criterion [2]. Left-hand side of the inequality holds amount of work done in the volume, V , by gas expansion due to heat release rate (if they are sufficiently in phase which means phase shift lies between -90 and 90 degrees) while the right-hand side term holds acoustic losses through boundaries. If the volume integral term exceeds the surface integral term, then acoustic oscillations are starting to increase. Numerous attempts has been made by engineers and researchers either to avoid acoustic pressure p' being in phase with q' or to increase the dissipation term on the boundaries.

1.3 Analyzing Thermoacoustic Instabilities

In the current literature, thermoacoustic problems are analysed by computational and experimental approaches, as usual. Computational framework consists of large eddy simulations (LES), network models and Helmholtz solvers.

1.3.1 Large Eddy Simulations

Computational fluid dynamics (CFD) simulations of thermoacoustic problems are mainly done by LES. LES results are useful to obtain flame transfer functions of the combustor. It plays an important role for Helmholtz solvers. However, LES requires high computational power to produce high fidelity results.

The compressible LES of turbulent swirled combustor is performed in [3]. In this study, the wave equation for reacting flow is derived and LES is performed to obtain flow variables. Mean temperature distribution and FTF data are extracted to be used as input for Helmholtz solver. Finally, most unstable thermoacoustic modes of combustor are determined using Helmholtz solver.

LES is also used for determining other thermoacoustic modes. The azimuthal modes of annular combustion chamber are investigated in [4] by LES and Helmholtz solver. Real

helicopter engine has taken into account and azimuthal modes are extracted by means of compressible LES and three dimensional Helmholtz solver.

Despite all of advantages of LES, simulation results may not guide about how to control or avoid thermoacoustic instabilities [5] qualitatively. It is possible to obtain reliable and accurate solution by LES, but the cost of computation is too high to analyse problem quantitatively, which could be useful for designing thermoacoustically stable combustor more quickly.

1.3.2 Helmholtz solvers

Since only considering acoustic field in frequency domain for combustors, Helmholtz solvers provide computationally efficient solution of thermoacoustic eigenmodes comparing to LES. It is also possible to handle complex valued impedance boundary conditions for two and three dimensional geometries with Helmholtz solvers. Computation of thermoacoustic modes for industrial burners via Helmholtz solvers shown in [6].

Juniper [7] proposed the effectiveness of adjoint methods by calculating the thermoacoustic eigenmode sensitivities which enable to observe the impact of each parameter by performing single calculation. The adjoint methods applied to the Helmholtz solver. Obtained sensitivities reveal the tendency to stabilization effect of each system parameter. Effect of the placement of the hot/cold mesh are also discussed by means of sensitivities of growth rate with respect to that parameter. It has been shown that adjoint based calculations can be leveraged to determine system parameter's effects on eigenvalue of the thermoacoustically unstable system. Consequently, adjoint methods could empower the capability of Helmholtz solver to optimize system quantitatively and quickly.

1.4 Thermoacoustic Modes

It would be informative to make a quick review about thermoacoustic modes in literature. There are two common eigenmodes occur in combustors; longitudinal and azimuthal. Longitudinal modes are mainly investigated to understand the thermoacoustic behaviour of single-burner combustors and benchmarking the implemented solvers against low order analytical results [8].

There are azimuthal thermoacoustic modes that can be exist in the combustors as well as longitudinal modes. The analytical approach to calculate azimuthal modes is given by Sun et. al.[9] for a simple annular chamber.

The comprehensive acoustic analysis on lean premixed prevaporized gas turbine combustors is performed by Dowling and Stow [10]. They built 1D network model with appropriate boundary conditions and the instabilities are calculated in frequency domain, then the obtained model is extended to simulate azimuthal modes which are dominant modes in annular combustors. The effects of mean flow, temperature gradients and heat release distribution have been analysed.

Extensive study on laboratory-scaled MICCA combustor has been conducted both numerically and experimentally in [11]. By constructing setup for a single burner, flame describing function (FDF) is found for two different operating conditions of bulk velocity and air/propane ratio. Since the found flame response represents certain operating points, the data is extrapolated in order to cover MICCA combustor's operation range. Then, obtained FDF is used in Helmholtz solver to predict spinning and standing azimuthal modes of annular combustor. It has been concluded that simulation results of stability analysis from Helmholtz solver and analytical solution are in good agreement.

Another study on azimuthal modes has been performed by Worth and Dawson [12]. The circumferential modes of laboratory-scaled annular combustor has been investigated experimentally. Effect of different flame separation distances on combustion instability is observed. It is indicated that resonance frequencies, amplitude of limit cycle and magnitude of heat release fluctuations are found to be increased by decreasing flame separation distances.

This quick review shows that Helmholtz solver successfully captures the eigenmodes of the combustors. Also parameters of complex combustor geometries can be analyzed more cheaply comparing to experimental studies.

1.5 Control Methods

Thermoacoustic instabilities are generally subjected to two control strategies; feedback control methods and passive control methods.

1.5.1 Feedback Control (Closed Loop Control)

Feedback control methods are consistently gets the acoustic pressure signals from combustion system, then necessary parameters are tuned and sent back to the combustor.

One of the earlier study for closed loop control of thermoacoustic instability is conducted by [13]. The feedback system is proposed by combination of loudspeaker, microphone, amplifier and phase-shifter, that leads more than 40dB reduction of pressure oscillations in Rijke tube.

Most comprehensive review has been conducted by Dowling and Morgans [14]. In this study, background information about feedback control systems and practical implementations are elaborated from laboratory-scale Rijke tube to full-scale industrial gas turbines.

However, complex nature of active control methods offer expensive and complicated solutions for instability problems that they cause operational difficulties. Subsequently, passive control techniques are commonly preferred to avoid operational complexity of active control methods.

1.5.2 Passive Control Methods

In contrast to feedback control methods, passive control methods are considered more applicable to incorporate into thermoacoustic systems. Perforated liners, Helmholtz resonators and baffles are extensively used in the gas turbine industry.

Considering aerodynamic performance, the effectiveness of the drum-like silencers in the thermoacoustic systems are demonstrated analytically in [15]. This study shows that the presence of silencer which consists of flexible membrane and backing cavity lead to decrement of natural resonance frequency and increment of phase angle difference between heat release rate and acoustic pressure fluctuations. It is noted that the length of silencer, tension of the flexible membrane and depth of the cavity are crucial parameters for enabling acoustic losses through membrane surface for Rijke tube.

The acoustic damping of perforated liners investigated experimentally and numerically by Zhao et.al.[16]. Effect of pipe length and bias flow rate is observed, and these parameters are handled in real time using a multiple-parameter tuning scheme. Agreed numerical and experimental results show that the optimum damping performance of perforated liners can be achieved for wide range of frequency.

It can be seen that geometrical changes have a significant effect on thermoacoustic stability of the combustors. For that reason, geometrical dimensions of the combustor geometry can be quantity of interest of shape optimization studies for thermoacoustic stability.

1.6 Motivation of the study

Main reference is [17] for this study. The Helmholtz solver will be extended to three dimensional realistic gas turbine combustors. Efficacy of the adjoint based shape optimization is wanted to be demonstrated for thermoacoustic stabilization for complex geometries. Furthermore, effect of the geometry of cooling holes wanted to be investigated for reducing the growth rate. To achieve this, more accurate FTF implementation in the code is aimed to be developed.

Moreover, current Helmholtz solver's performance will be improved using efficient algorithms for matrix generation and parallelization. In this way, quantitative analysis would be obtained much more quickly.

Chapter 2

Mathematical Model of Thermoacoustic Instability

This chapter describes the derivation of thermoacoustic Helmholtz equation and discussion of boundary conditions and flame response.

2.1 Thermoacoustic Helmholtz Equation

Derivation of thermoacoustic governing equations is based on the conservation laws of mass, momentum and entropy for an ideal gas. The flow of derivation follows the methodology of [6].

To initiate the derivation, balance equations for mass, momentum and entropy can be written in inviscid form;

$$\frac{\partial \rho}{\partial t} + \nabla \cdot (\rho \mathbf{u}) = 0 \quad (2.1a)$$

$$\frac{\partial \rho \mathbf{u}}{\partial t} + \nabla \cdot (\rho \mathbf{u} \mathbf{u}) + \nabla p = 0 \quad (2.1b)$$

$$\frac{\partial s}{\partial t} + \mathbf{u} \cdot \nabla s = \frac{q}{\rho T} \quad (2.1c)$$

where t represents time, \mathbf{u} is velocity vector, p is pressure, s is entropy, T is temperature and q is heat release rate per unit volume. These transport equations represent the time dependent/independent variations of flow variables within corresponding physical domain.

The equations in (2.1) can be linearized through decomposition of flow variables. Each variable can be decomposed into two distinct parts; mean part(subscripted by 0 - order $\mathcal{O}(1)$) and fluctuating part (subscripted by 1 -order $\mathcal{O}(\varepsilon)$);

$$p(\mathbf{x}, t) = p_0(\mathbf{x}) + p_1(\mathbf{x}, t) \quad (2.2a)$$

$$\rho(\mathbf{x}, t) = \rho_0(\mathbf{x}) + \rho_1(\mathbf{x}, t) \quad (2.2b)$$

$$\mathbf{u}(\mathbf{x}, t) = \mathbf{u}_0(\mathbf{x}) + \mathbf{u}_1(\mathbf{x}, t) \quad (2.2c)$$

$$T(\mathbf{x}, t) = T_0(\mathbf{x}) + T_1(\mathbf{x}, t) \quad (2.2d)$$

$$q(\mathbf{x}, t) = q_0(\mathbf{x}) + q_1(\mathbf{x}, t) \quad (2.2e)$$

$$s(\mathbf{x}, t) = s_0(\mathbf{x}) + s_1(\mathbf{x}, t) \quad (2.2f)$$

These perturbations are applied to equation (2.1) by making following assumptions;

- Gas is assumed as perfect gas
- Governing equations should be satisfied for mean flow field.
- Viscous terms and volume forces neglected.
- Mean flow field is not time dependant.
- Only first order perturbations terms are kept, second and higher order terms are neglected. (The high order perturbations are very small comparing to mean flow variables.)

In addition to assumptions above, the zero Mach number mean flow assumption($\mathbf{u}_0(\mathbf{x}) \approx 0$) is imposed for further simplification of equation (2.1)(for details, see Appendix A of [6]). Once the mean flow velocity vector $\mathbf{u}_0(\mathbf{x}) \approx 0$, equation (2.1) gives that the gradient of mean pressure(∇p_0) and volumetric heat release rate (q_0) are zero. The linearized governing equations for perturbed quantities become;

$$\frac{\partial \rho_1}{\partial t} + \nabla \cdot (\rho_0 \mathbf{u}_1) = 0 \quad (2.3a)$$

$$\rho_0 \frac{\partial \mathbf{u}_1}{\partial t} + \nabla p_1 = 0 \quad (2.3b)$$

$$\frac{\partial s_1}{\partial t} + \mathbf{u}_1 \cdot \nabla s_0 = \frac{q_1}{\rho_0 T_0} \quad (2.3c)$$

These three balance equations in (2.3) can be combined in terms of each other. To obtain one single equation by combining them, rigorous analysis is needed including perfect gas relations. If the perfect gas law $p = \rho RT$ written in total differential form;

$$dp = d\rho RT + \rho R dT \implies \frac{dp}{T} = \rho R \frac{dT}{T} + R d\rho \implies \frac{dp}{p} = \frac{dT}{T} + \frac{d\rho}{\rho} \quad (2.4)$$

The perturbations in (2.2) are applied to (2.4) and by keeping all the first order terms(ϵ), it leads to

$$\frac{p_1}{p_0} = \frac{T_1}{T_0} + \frac{\rho_1}{\rho_0} \quad (2.5)$$

The first principle of the thermodynamics holds following entropy relation;

$$\frac{ds}{dt} = \frac{c_v}{p} \frac{dp}{dt} - \frac{c_p}{\rho} \frac{d\rho}{dt} \quad (2.6)$$

Then, integrating (2.6) reads;

$$s - s_0 = c_v \ln\left(\frac{p}{p_0}\right) - c_p \ln\left(\frac{\rho}{\rho_0}\right) \implies \frac{p}{p_0} = \exp\left(\frac{s - s_0}{c_v}\right) \left(\frac{\rho}{\rho_0}\right)^\gamma \quad (2.7)$$

Applying Taylor series expansion while keeping only first order terms results in;

$$p(\rho_0 + \rho_1, s_0 + s_1) = p(\rho_0, s_0) + \left.\frac{\partial p}{\partial \rho}\right|_{\rho_0, s_0} (\rho - \rho_0) + \left.\frac{\partial p}{\partial s}\right|_{\rho_0, s_0} (s - s_0) \quad (2.8)$$

where $\rho = \rho_0 + \rho_1$. Partial derivatives of p with respect to density and entropy are;

$$\left.\frac{\partial p}{\partial \rho}\right|_{\rho_0, s_0} = \gamma \frac{p_0}{\rho_0} \quad , \quad \left.\frac{\partial p}{\partial s}\right|_{\rho_0, s_0} = \frac{p_0}{c_v} \quad (2.9)$$

Substitution of terms in equation (2.9) into equation (2.8) yields;

$$p_1 + p_0 = p_0 + \gamma \frac{p_0}{\rho_0} ((\rho_0 + \rho_1) - \rho_0) + \frac{p_0}{c_v} ((s_0 + s_1) - s_0) \quad (2.10)$$

Dividing both side with p_0 gives the relation for s_1 ;

$$\frac{p_1}{p_0} = \gamma \frac{\rho_1}{\rho_0} + \frac{s_1}{c_v} \quad (2.11)$$

Reconsidering the equation (2.6) based on the resting mean flow assumption, pressure gradient would be neglected $\nabla p_0 \approx 0$. Since the problem is time-independent, equation (2.6) can be rewritten as;

$$\nabla s_0 = \frac{c_v}{p_0} \nabla p_0 - \frac{c_p}{\rho} \nabla \rho_0 \approx -\frac{c_p}{\rho} \nabla \rho_0 \quad (2.12)$$

Introducing equation (2.12) into equation (2.3c) gives;

$$\frac{\partial s_1}{\partial t} - \mathbf{u}_1 \frac{c_p}{\rho_0} \nabla \rho_0 = \frac{r q_1}{p_0} \implies \frac{1}{c_p} \frac{\partial s_1}{\partial t} - \frac{\mathbf{u}_1}{\rho_0} \nabla \rho_0 = \frac{R q_1}{c_p p_0} \quad (2.13)$$

From relation (2.11), ρ_1 can be obtained and the partial derivative with respect to time reads;

$$\rho_1 = \frac{\rho_0}{\gamma} \left(\frac{p_1}{p_0} - \frac{s_1}{c_v} \right) \implies \frac{\partial \rho_1}{\partial t} = \frac{\rho_0}{\gamma p_0} \frac{\partial p_1}{\partial t} - \frac{\rho_0}{c_p} \frac{\partial s_1}{\partial t} \quad (2.14)$$

Inserting equation (2.14) into (2.3a) and using (2.13) yields;

$$\frac{1}{\gamma p_0} \frac{\partial p_1}{\partial t} + \nabla \mathbf{u}_1 = \frac{R q_1}{c_p p_0} \quad (2.15)$$

Taking time derivative of (2.15) and equation (2.3b) over ρ_0 leads;

$$\frac{1}{\gamma p_0} \frac{\partial p_1}{\partial t^2} - \nabla \cdot \left(\frac{1}{\rho_0} \nabla p_1 \right) = \frac{\gamma - 1}{\gamma p_0} \frac{\partial q_1}{\partial t} \quad (2.16)$$

Substitution of $c = \sqrt{\gamma p_0 / \rho_0}$, equation (2.16) can be written equivalently as;

$$\frac{\partial p_1}{\partial t^2} - \nabla \cdot (c^2 \nabla p_1) = (\gamma - 1) \frac{\partial q_1}{\partial t} \quad (2.17)$$

Analysing (2.17) can be much more manageable by transforming the variables from time domain into frequency domain. Then harmonic variables can be defined concisely;

$$p_1(\mathbf{x}, t) = \text{Re} \{ \hat{p}(\mathbf{x}) e^{-i\omega t} \} \quad (2.18a)$$

$$\mathbf{u}_1(\mathbf{x}, t) = \text{Re} \{ \hat{\mathbf{u}}(\mathbf{x}) e^{-i\omega t} \} \quad (2.18b)$$

$$q_1(\mathbf{x}, t) = \text{Re} \{ \hat{q}(\mathbf{x}) e^{-i\omega t} \} \quad (2.18c)$$

where ω denotes complex angular frequency of the acoustic wave, its real part ω_r is angular frequency and imaginary part ω_i is growth rate of the acoustic wave. Hence inhomogeneous acoustic wave equation in frequency domain;

$$\nabla \cdot (c^2 \nabla \hat{p}) + \omega^2 \hat{p} = i\omega(\gamma - 1) \hat{q} \quad (2.19)$$

The equation (2.19) is called inhomogeneous Helmholtz equation. If eigenvalue ω has positive growth rate $\omega_i > 0$, then oscillating term ($e^{-i\omega t}$) in (2.18) grows exponentially, then the amplitude of the acoustic waves grows in time which leads thermoacoustic instability.

2.2 Source Term in Helmholtz Equation

The formulation for \hat{q} in (2.19) has been adopted from [7];

$$\hat{q} = \frac{Q}{U_b} v(\mathbf{x}) F(\omega) \int w(\zeta) \hat{\mathbf{u}}(\mathbf{x}) \cdot \mathbf{n}_r dV \quad (2.20)$$

where integrals of $\int v dV$ and $\int w dV$ are equal to 1, Q is total heat power of the flame and U_b is the bulk velocity of the flow domain, w and h are measurement and heat release distributions and $F(\omega)$ is the flame transfer function. In the case of w is specified as Dirac-delta function δ_D , substitution of $\hat{\mathbf{u}}(\mathbf{x})$ with ∇p by using (2.19) and frequency domain form of (2.3b) gives;

$$\hat{q} = \frac{Q}{U_b} v(\mathbf{x}) F(\omega) \hat{\mathbf{u}}(\mathbf{x}_r) \cdot \mathbf{n}_r = \frac{Q}{U_b} \frac{1}{i\omega\rho(\mathbf{x}_r)} v(\mathbf{x}) F(\omega) \nabla \hat{p}(\mathbf{x}_r) \cdot \mathbf{n}_r \quad (2.21)$$

Therefore, Helmholtz equation (2.19) with the source term becomes;

$$\nabla \cdot (c^2 \nabla \hat{p}) + \omega^2 \hat{p} = \frac{Q}{U_b} \frac{(\gamma - 1)}{\rho(\mathbf{x}_r)} v(\mathbf{x}) F(\omega) \nabla \hat{p}(\mathbf{x}_r) \cdot \mathbf{n}_r \quad (2.22)$$

2.3 Flame Transfer Function (FTF)

Flame transfer function describes the relationship between heat release rate fluctuations and acoustic field of the combustors to determine existing unstable modes [18]. These relation is essential input for the acoustic Helmholtz solvers, to model flame response in frequency domain [5]. Frequently used FTF is $n - \tau$ formulation [19];

$$Q = nu'(t - \tau) \quad (2.23)$$

where $n = NQ/U_b$ is dimensional interaction index, τ is the convection time of the velocity fluctuations at injection plane to trigger heat release fluctuations [4]. Similarly, if the Fourier transform applied to (2.23) and FTF can be extracted as;

$$F(\omega) = Ne^{i\omega\tau} \quad (2.24)$$

where N denotes non-dimensional interaction index which is also magnitude of the FTF while $\omega\tau$ is phase. Spatial distribution of these parameters' (n, τ) fields can be obtained through

experiments and LES simulations [3]. If n is zero, the case is called *passive flame* since there is no source term for Helmholtz equation. Otherwise, it is called *active flame* case which has non-zero interaction index, therefore unsteady heat release component comes into play. These two cases will be taken into account while deriving the finite element models in §3.

2.4 Boundary Conditions for Helmholtz Equation

In thermoacoustic instability problems, there are three common boundary conditions used as usual, Dirichlet (open boundary), Neumann (closed boundary) and Robin (arbitrary impedance) [20].

Acoustic impedance Z , is a ratio of emitted energy by pressure and energy impeded on surface. The specific impedance defined as Fourier transformed signal reads;

$$Z = \frac{\hat{p}}{\rho_0 c_0 \hat{\mathbf{u}} \cdot \mathbf{n}_s} \quad (2.25)$$

To start with, some point allocated at surface S with unit normal vector \mathbf{n}_s pointing into the surface (Generally, unit vector are defined as pointing out the surface S). \hat{p} is the acoustic field and \mathbf{u} is acoustic velocity. If specific acoustic impedance is a complex number $Z(\omega) = \Re(\omega) + i\Im(\omega)$, the real part \Re is acoustic resistance and imaginary part \Im is acoustic reactance. The imaginary part of the impedance plays a key role to characterize the phase angle between acoustic pressure(\hat{p}) and heat release fluctuations(\hat{q}).

It should be noted that Z cannot be considered as the property of surface due to the existence of acoustic field \hat{p} . Also Z can be represented by reflection coefficient Γ ; $Z = (1 + \Gamma)/(1 - \Gamma)$. The inverse of Z is called admittance, Y .

Mathematically speaking, impedance is considered as "Robin" boundary condition. If (2.3b) is considered in frequency domain and inserting (2.25) into that relation gives Robin boundary condition for thermoacoustic problem;

$$\nabla \hat{p} \cdot \mathbf{n} - \frac{i\omega}{cZ} \hat{p} = 0 \quad (2.26)$$

Equation (2.26) consists all boundary conditions by considering different scenarios;

1. For open ends (Dirichlet), the limit Z goes to 0, then $\hat{p} = 0$.
2. For closed ends (Neumann), the limit Z goes to infinity due to velocity \mathbf{u} is zero on the rigid wall. Hence, $\nabla \hat{p} = 0$.
3. For arbitrary impedance case, the limit Z neither goes infinity nor zero. Therefore, Robin boundary conditions applies which simulates acoustic radiation from boundaries.

Chapter 3

Finite Element Based Helmholtz Solver

In this chapter, the implementation of discretized forms of equations and eigenvalue solver will be addressed.

The derived thermoacoustic Helmholtz equation is served as "main" equation to model thermoacoustic behaviour for the given physical situation, geometry and boundary conditions. Finite difference, finite volume or finite element methods can be utilized to perform numerical simulations of model equation (2.19)[7].

As mentioned in previous chapter, three possible boundary conditions are considered for any given domain Ω , then problem can be represented as;

$$\nabla \cdot (c^2 \nabla \hat{p}) + \omega^2 \hat{p} = \frac{Q}{U_b} \frac{(\gamma - 1)}{\rho(\mathbf{x}_r)} v(\mathbf{x}) F(\omega) \nabla \hat{p}(\mathbf{x}_r) \cdot \mathbf{n}_r \quad \text{in } \Omega \quad (3.1)$$

and its boundaries $\partial\Omega_D$ for Dirichlet boundary, $\partial\Omega_N$ for Neumann boundary, and $\partial\Omega_R$ for Robin boundary;

$$\hat{p} = 0 \quad \text{on } \partial\Omega_D \quad (3.2a)$$

$$\frac{\partial \hat{p}}{\partial n} = 0 \quad \text{on } \partial\Omega_N \quad (3.2b)$$

$$\frac{\partial \hat{p}}{\partial n} - \frac{i\omega}{cZ} \hat{p} = 0 \quad \text{on } \partial\Omega_R \quad (3.2c)$$

Since combustor geometries have complex shape, finite element method is utilized to discretization of (3.1). The corresponding weak forms are derived in order to represent the thermoacoustic problem as nonlinear eigenvalue problem. Then, obtained matrix system can be solved by iterative solvers.

3.1 Finite Element Method Definitions

Galerkin finite element method is used to discretize the problem domain. Continuous Galerkin finite elements are built in Lebesgue space L_2 . If the test and trial functions are defined in that function space can be denoted as u and v , the inner product definition becomes;

$$\langle u | v \rangle = \int_{\Omega} u^* v dV \quad (3.3)$$

also L_2 norm is;

$$\| u \| = \sqrt{\int_{\Omega} u^* u dV} = \sqrt{\langle u | u \rangle} \quad (3.4)$$

superscript * denotes complex conjugate of function.

3.2 Passive Flame Discretization

Firstly, derivation for passive flame case (mentioned in §2.3) will be performed. If the source term of the thermoacoustic Helmholtz equation is not considered, pure acoustic behaviour of the domain can be obtained. The relevant form of (2.19) reads;

$$\nabla \cdot (c^2 \nabla \hat{p}) + \omega^2 \hat{p} = 0 \quad \text{in } \Omega \quad (3.5)$$

Let's focus on the first term and equate this to f by letting $c^2 \nabla \hat{p} = w$;

$$f = \nabla \cdot (c^2 \nabla \hat{p}) = \nabla \cdot w \quad (3.6)$$

To derive variational formulation of f , it is required to multiply both sides with complex conjugate of the test function (v^*) and integrate utilizing Green's formula yields;

$$\int_{\Omega} f v^* d\mathbf{x} = \int_{\Omega} (\nabla \cdot w) v^* d\mathbf{x} \quad (3.7a)$$

$$\int_{\Omega} f v^* d\mathbf{x} = - \int_{\Omega} w \cdot \nabla v^* d\mathbf{x} + \int_{\partial\Omega} (w \cdot \mathbf{n}) v^* d\sigma \quad (3.7b)$$

Inserting relation $w = c^2 \nabla \hat{p}$ back into equation (3.7) reads;

$$\int_{\Omega} f v^* d\mathbf{x} = - \int_{\Omega} (c^2 \nabla \hat{p}) \cdot \nabla v^* d\mathbf{x} + \int_{\partial\Omega} ((c^2 \nabla \hat{p}) \cdot \mathbf{n}) v^* d\sigma \quad (3.8)$$

The second term on the right-hand side of the (3.8) is boundary integral which represents the Robin boundary condition. Trial function introduced as \hat{p} with complex coefficients \hat{p}_j and basis functions $\phi_j(\mathbf{x})$, $\hat{p}_h = \sum_{j=1}^N \hat{p}_j \phi_j(\mathbf{x})$. Test function can also be defined as $v = \{\phi_k\}_{k=1}^N$, therefore trial function and test function can be substituted into equation (3.8);

$$\begin{aligned} \int_{\Omega} f v^* \, d\mathbf{x} &= - \int_{\Omega} c^2 \nabla \left(\sum_{j=1}^N \hat{p}_j \phi_j(\mathbf{x}) \right) \cdot \nabla \phi_k \, d\mathbf{x} + \int_{\partial\Omega} \left(c^2 \nabla \left(\sum_{j=1}^N \hat{p}_j \phi_j(\mathbf{x}) \right) \cdot \mathbf{n} \right) \phi_k \, d\sigma \\ &= - \sum_{j=1}^N \int_{\Omega} (c^2 \nabla (\phi_j(x)) \cdot \nabla \phi_k \, d\mathbf{x} \hat{p}_j + \sum_{j=1}^N \int_{\partial\Omega} (c^2 \nabla \phi_j(x) \cdot \mathbf{n}) \phi_k \, d\sigma \hat{p}_j \end{aligned} \quad (3.9)$$

Equation (3.9) defines the weak formulation of first term of (3.1). The second integral of (3.9) states Robin boundary condition integral;

$$\sum_{j=1}^N \int_{\partial\Omega} (c^2 \nabla \phi_j(x) \cdot \mathbf{n}) \phi_k \, d\sigma \hat{p}_j \quad (3.10)$$

Recalling the (2.25) and introduce this relation into Robin boundary condition equation (2.26) gives;

$$\nabla \hat{p} \cdot \mathbf{n} - \frac{i\omega}{cZ} = 0 \implies \nabla \hat{p} \cdot \mathbf{n} = \frac{i\omega \hat{p}}{cZ} = \frac{i\omega}{cZ} \sum_{j=1}^N \hat{p}_j \phi_j(x) \quad (3.11)$$

Similar to definition of trial function above, its gradient can be written as $\nabla \hat{p}_h = \sum_{j=1}^N \hat{p}_j \nabla \phi_j(\mathbf{x})$. Therefore, (3.11) becomes

$$\sum_{j=1}^N \hat{p}_j \nabla \phi_j(x) \cdot \mathbf{n} = \frac{i\omega}{cZ} \sum_{j=1}^N \hat{p}_j \phi_j(x) \implies \sum_{j=1}^N \nabla \phi_j(x) \cdot \mathbf{n} = \frac{i\omega}{cZ} \sum_{j=1}^N \phi_j(x) \quad (3.12)$$

Substituting of (3.12) into (3.10), (3.9) can be written in terms of test and trial functions without evaluating their gradients;

$$\int_{\Omega} f v^* \, d\mathbf{x} = - \sum_{j=1}^N \int_{\Omega} c^2 \nabla \phi_j \cdot \nabla \phi_k \, d\mathbf{x} \hat{p}_j + \sum_{j=1}^N \int_{\partial\Omega} \left(c \frac{i\omega}{Z} \right) \phi_j \phi_k \, d\sigma \hat{p}_j \quad (3.13)$$

Finally, substitution of test and trial functions for second term of (3.5) and integrating this term over the domain gives the complete variational form of (3.5);

$$-\sum_{j=1}^N \int_{\Omega} c^2 \nabla \phi_j \cdot \nabla \phi_k \, d\mathbf{x} \hat{p}_j + \omega \sum_{j=1}^N \int_{\partial\Omega} \left(\frac{ic}{Z} \right) \phi_j \phi_k \, d\sigma \hat{p}_j + \omega^2 \sum_{j=1}^N \int_{\Omega} \phi_j \phi_k \, d\mathbf{x} \hat{p}_j = 0$$

(for $k = 1, 2, 3, \dots, N$) (3.14)

If each relation in summations in (3.14) represented as symmetric matrices;

$$\mathbf{A}_{jk} = - \int_{\Omega} c^2 \nabla \phi_j \cdot \nabla \phi_k \, d\mathbf{x} \quad (3.15a)$$

$$\mathbf{B}_{jk} = \int_{\partial\Omega} \left(\frac{ic}{Z} \right) \phi_j \phi_k \, d\sigma \quad (3.15b)$$

$$\mathbf{C}_{jk} = \int_{\Omega} \phi_j \phi_k \, d\mathbf{x} \quad (3.15c)$$

Therefore, the quadratic eigenvalue problem is obtained;

$$\mathbf{A}\mathbf{p} + \omega\mathbf{B}\mathbf{p} + \omega^2\mathbf{C}\mathbf{p} = 0 \quad (3.16)$$

where \mathbf{A} and \mathbf{C} are real matrices while \mathbf{B} is complex (except in the case of Z has real part of zero, $Z = 0 + bi$), ω denotes eigenvalues of the eigenvalue problem and \mathbf{p} is corresponding eigenfunctions that satisfy (3.16).

3.3 Active Flame Discretization

For active flame discretization, the weak formulation of left-hand side of (3.1) stays same and additional weak formulation should be derived for source term. The relation to be discretized is;

$$\frac{Q}{U_b} \frac{(\gamma-1)}{\rho(\mathbf{x}_r)} v(\mathbf{x}) F(\omega) \nabla \hat{p}(\mathbf{x}_r) \cdot \mathbf{n}_r \quad (3.17)$$

Similarly, (3.17) can be multiplied with test function $\{\phi_k\}_{k=1}^N$ and gradient of the trial function $\nabla \hat{p}_h(\mathbf{x}_r)$ can be substituted with $\sum_{j=1}^N \hat{p}_j \nabla \phi_j(\mathbf{x}_r)$. Next, integration over the domain Ω gives;

$$\sum_{j=1}^N \left(\frac{Q}{U_b} \frac{(\gamma-1)}{\rho(\mathbf{x}_r)} F(\omega) \int_{\Omega} v(\mathbf{x}) \phi_k \, dV \nabla \phi_j(\mathbf{x}_r) \cdot \mathbf{n}_r \right) \hat{p}_j \quad (\text{for } k = 1, 2, 3, \dots, N) \quad (3.18)$$

Then the matrix \mathbf{D} can be defined as;

$$\mathbf{D}_{kj}(\omega) = \underbrace{\frac{Q}{U_b} \frac{(\gamma-1)}{\rho(\mathbf{x}_r)} F(\omega)}_{\text{coefficient}} \int_{\Omega} v(\mathbf{x}) \phi_k dV \nabla \phi_j(\mathbf{x}_r) \cdot \mathbf{n}_r \quad (\text{for } k = 1, 2, 3, \dots, N) \quad (3.19)$$

For operational simplicity, cross product between $\int_{\Omega} v(\mathbf{x}) \phi_k dV$ and $\nabla \hat{\phi}_j(\mathbf{x}_r) \cdot \mathbf{n}_r$ is performed, and found matrix is multiplied with the other terms that are considered as constant labelled *coefficient*.

3.4 Solution of Quadratic Eigenvalue Problem

Equation (3.16) can be solved by SLEPc (Scalable Library for Eigenvalue Problem Computations)[21]. SLEPc provides a bunch of eigenvalue solvers for linear and nonlinear eigenvalue problems. Most of the case, the requested number of eigenvalues and left/right eigenvectors can be easily computed via these solvers.

The composition of (3.16) and (3.19) leads to quadratic eigenvalue problem with right-hand side;

$$\mathbf{A}\mathbf{p} + \omega\mathbf{B}\mathbf{p} + \omega^2\mathbf{C}\mathbf{p} = \mathbf{D}(\omega)\mathbf{p} \implies [(\mathbf{A} - \mathbf{D}(\omega)) + \omega\mathbf{B} + \omega^2\mathbf{C}] \mathbf{p} = 0 \quad (3.20)$$

This equation cannot be solved by traditional linear algebraic methods since the equation is strongly nonlinear because of the flame matrix $\mathbf{D}(\omega)$. Hence, it should be represented as generalized nonlinear eigenvalue problem to solve it iteratively;

$$[(\mathbf{A} - \mathbf{D}(\omega_{k-1})) + \omega_k\mathbf{B} + \omega_k^2\mathbf{C}] \mathbf{p} = 0 \quad (3.21)$$

where k is the iteration number. Nicoud's fixed point iteration is well-suited approach to tackle with this nonlinear eigenvalue problem[6].

Short description of fixed point iteration is presented as pseudocode in Algorithm 1.

Algorithm 1 Fixed Point Iteration

```

1: function FIXED POINT ITERATION(A, B, C, D, tol, maxiter)
2:    $k \leftarrow -1$ 
3:    $\alpha^0 \leftarrow 0.5$ 
4:    $\omega^{|k|} \leftarrow 0$ 
5:   Determine  $\omega^{|k+1|}$  using A, B, C
6:    $\Delta\omega \leftarrow 2 \times tol$ 
7:   while  $|\Delta\omega| > tol$  and  $k < maxiter$  do
8:      $k \leftarrow k + 1$ 
9:     Assemble D( $\omega^{|k|}$ )
10:    N  $\leftarrow$  A - D( $\omega^{|k|}$ )
11:    Determine  $\omega^{|k+1|}$  using N, B, C
12:    if  $k \neq 0$  then
13:       $\alpha^k \leftarrow \frac{1}{(1 - (\omega^{|k|} - \omega^{|k+1|}))(\omega^{|k|} - \omega^{|k+1|})}$ 
14:    end if
15:     $\omega^{|k+1|} = \alpha^k * \omega^{|k|} + (1 - \omega^{|k|}) \times \omega^{|k|}$ 
16:     $|\Delta\omega| \leftarrow \left| \omega^{|k+1|} - \omega^{|k|} \right|$ 
17:  end while
18:  return Eigenvalue  $\omega^{|k+1|}$  and Eigenvector p
19: end function

```

3.5 Implemented Helmholtz Solver

Implemented Helmholtz solver exploits PETSc[22] and SLEPc[21] libraries extensively. The proposed methodology to compute eigenmodes of thermoacoustic system is shown in Figure 3.1. As usual, process starts with generation of geometry and mesh by means of Gmsh[23] using Delaunay-triangulation. The matrices are generated using finite element libraries Dofin and Dofinx. Then boundary conditions are imposed to predefined boundary faces/lines. Next, relevant matrices are assembled according to boundary conditions. After switching the flame mode as on/off the eigensolver SLEPc object is obtained which comprises eigenvalue and direct/adjoint eigenvectors. Finally, eigenvectors can be post-processed using Paraview[24].

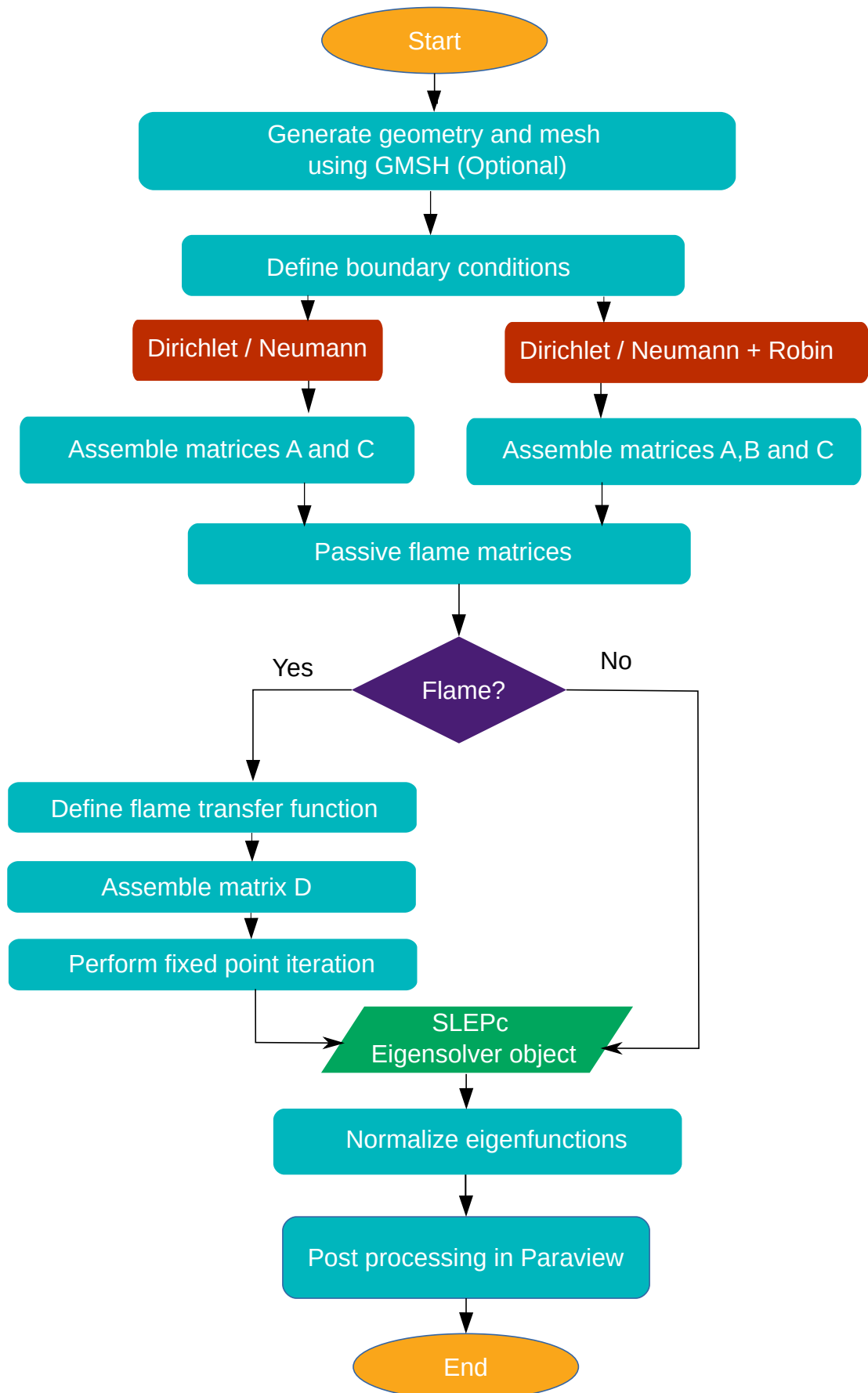


Fig. 3.1 Proposed Methodology

Chapter 4

Sensitivity of the Eigenvalue with Adjoint

The finite element model is developed for thermoacoustic Helmholtz equation in previous chapter. In this chapter, the same problem is considered with adjoint approach.

The adjoint formulation enables to determine physical behaviours of the system variables more cheaply[7]. The effect of changes in thermoacoustic system variables on eigenvalue of the system becomes quantity of interest. Comparing to traditional finite difference methods, gradient information can be calculated inexpensively for each system parameter using adjoint method. Only one single calculation, these gradients can be calculated via appropriate formulation of (3.20).

This chapter starts with introduction of left eigenvector (adjoint operator). Secondly, base state sensitivities of the flow variables are derived. Thirdly, shape sensitivities for different boundary conditions is presented. Lastly, Taylor remainder test is described briefly.

4.1 Left Eigenvector

For any given linear operator \mathcal{L} , the definition of adjoint for any given vectors \mathbf{p}^\dagger and \mathbf{p} ;

$$\langle \mathbf{p}^\dagger | \mathcal{L}\mathbf{p} \rangle = \langle \mathcal{L}^\dagger \mathbf{p}^\dagger | \mathbf{p} \rangle + \text{boundary terms} \quad (4.1)$$

Equation (3.21) represents the generalized nonlinear eigenvalue problem. If premultiplier \mathbf{p}^\dagger is introduced to this equation;

$$\mathbf{p}^\dagger [(\mathbf{A} - \mathbf{D}(\omega)) + \omega\mathbf{B} + \omega^2\mathbf{C}] \mathbf{p} = 0 \quad (4.2)$$

In equation (4.2), \mathbf{p}^\dagger is called adjoint eigenfunction which satisfies equation (4.2) for arbitrary \mathbf{p} . And \mathbf{p} is called direct eigenfunction which holds the right eigenvector considering equation (3.21).

The matrix form of the direct equation (3.21) reads;

$$[(\mathbf{A} - \mathbf{D}(\omega)) + \omega\mathbf{B} + \omega^2\mathbf{C}] \mathbf{p} = \mathbf{L}(\omega)\mathbf{p} = 0 \quad (4.3)$$

Considering definition (4.1);

$$(\mathbf{p}^\dagger)^H \mathbf{L}(\omega)\mathbf{p} = (\mathbf{L}(\omega)^H \mathbf{p}^\dagger)^H \mathbf{p} = (\mathbf{L}^\dagger(\omega^*)\mathbf{p}^\dagger)^H \mathbf{p} = 0 \quad (4.4)$$

Then adjoint formulation of the problem yields;

$$\mathbf{L}^\dagger(\omega^*)\mathbf{p}^\dagger = [(\mathbf{A} - \mathbf{D}(\omega)^H) + \omega^*\mathbf{B}^H + \omega^{*2}\mathbf{C}] \mathbf{p}^\dagger = 0 \quad (4.5)$$

where superscript H denotes complex conjugation and subscript $*$ denotes complex conjugate of the eigenvalue ω . Since they contain imaginary components in their formulations, matrix \mathbf{B} and matrix \mathbf{D} requires complex conjugation while matrices \mathbf{A} and \mathbf{C} remain self-adjoint. By looking closer to the equations (4.3) and (4.5), it can be concluded that left eigenvectors of the direct problem becomes the right eigenvectors of the adjoint problem.

4.2 Base State Sensitivities

If the eigenvalue problem $\mathcal{L}(\omega)\hat{p} = 0$ is perturbed as $\mathcal{L} + \varepsilon\delta\mathcal{L}$, then perturbed eigenvalue and eigenfunction terms yields;

$$\mathcal{L}(\omega + \varepsilon\delta\omega)(\hat{p} + \varepsilon\delta\hat{p}) + \varepsilon\delta\mathcal{L}(\omega)(\hat{p} + \varepsilon\delta\hat{p}) = 0 \quad (4.6)$$

The first order Taylor-series approximation is applied to first term, then $\mathcal{L}(\omega + \varepsilon\delta\omega)$ becomes $\mathcal{L}(\omega) + \partial\mathcal{L}(\omega)/\partial\omega|_\omega\varepsilon\delta\omega$. This inserted into equation (4.6) with keeping only first order(ε) terms;

$$\mathcal{L}(\omega)\delta\hat{p} + \frac{\partial\mathcal{L}(\omega)}{\partial\omega}|_\omega\delta\omega\hat{p} + \delta\mathcal{L}(\omega)\hat{p} = 0 \quad (4.7)$$

The equation (4.7) is multiplied by adjoint eigenvector \hat{p}^\dagger and integrate over the domain by considering the inner product definition of $\langle \mathbf{v} | \mathbf{u} \rangle = \langle \mathbf{v}^H | \mathbf{u} \rangle$ in matrix form reads;

$$\mathbf{p}^{\dagger H} \mathbf{L}(\omega)\mathbf{p} + \mathbf{p}^{\dagger H} \frac{\partial\mathbf{L}(\omega)}{\partial\omega}|_\omega\delta\omega\mathbf{p} + \mathbf{p}^{\dagger H} \delta\mathbf{L}(\omega)\mathbf{p} = 0 \quad (4.8)$$

Since $\mathbf{p}^{\dagger H} \mathbf{L}(\omega) \mathbf{p} = (\mathbf{L}^H(\omega) \mathbf{p}^{\dagger})^H \mathbf{p}$, the leftmost element of equation (4.8) becomes zero. Therefore, by arranging the terms in equation (4.8), first order eigenvalue problem yields as;

$$\delta\omega = -\frac{\mathbf{p}^{\dagger H} \delta\mathbf{L}(\omega) \mathbf{p}}{\mathbf{p}^{\dagger H} \frac{\partial \mathbf{L}(\omega)}{\partial \omega} |_{\omega} \mathbf{p}} \quad (4.9)$$

where perturbed matrices in perturbed operator $\delta\mathbf{L}(\omega)$ are;

$$\delta\mathbf{A}_{jk} = -\int_{\Omega} 2\bar{c} \delta\bar{c} \nabla \phi_j \cdot \nabla \phi_k d\mathbf{x} = -\int_{\Omega} \delta\bar{v}(\mathbf{x}) \gamma p_{amb} \nabla \phi_j \cdot \nabla \phi_k d\mathbf{x} \quad (4.10a)$$

$$\delta\mathbf{B}_{jk} = -\int_{\partial\Omega} \left(\frac{i\bar{c} \delta Z}{Z^2} \right) \phi_j \phi_k d\sigma \quad (4.10b)$$

$$\delta\mathbf{C}_{jk} = 0 \quad (4.10c)$$

$$\begin{aligned} \delta\mathbf{D}_{kj} &= \frac{\dot{Q}_t}{U_b \rho(\mathbf{x}_r)} (\gamma - 1) \delta n e^{i\omega_0 \tau} \int_{\Omega} \phi_k dV \nabla \phi_j(\mathbf{x}_r) \cdot \mathbf{n}_r \\ &+ i\omega \frac{\dot{Q}_t}{U_b \rho(\mathbf{x}_r)} (\gamma - 1) n \delta \tau e^{i\omega \tau} \int_{\Omega} \phi_k dV \nabla \phi_j(\mathbf{x}_r) \cdot \mathbf{n}_r \\ &+ \frac{\dot{Q}_t 2\bar{c}(\mathbf{x}_r) \delta\bar{c}(\mathbf{x}_r)}{U_b p_{amb}} \frac{(\gamma - 1)}{\gamma} n e^{i\omega \tau} \int_{\Omega} \phi_k dV \nabla \phi_j(\mathbf{x}_r) \cdot \mathbf{n}_r \end{aligned} \quad (4.10d)$$

In perturbed matrix $\delta\mathbf{B}$, the effect of speed of sound perturbation \bar{c} is neglected. It is easily shown that the derivative of the operator \mathcal{L} with respect to eigenvalue is;

$$\frac{\partial \mathbf{L}(\omega)}{\partial \omega} |_{\omega} = -\frac{\partial \mathbf{D}(\omega)}{\partial \omega} |_{\omega} + \frac{\partial \mathbf{B}}{\partial \omega} + 2\omega \frac{\partial \mathbf{C}}{\partial \omega} \quad (4.11)$$

Now, sensitivity of the eigenvalue with respect to base state quantities such as n , τ , \bar{c} can be written. These parameters are scalar apart from the speed of sound \bar{c} which is a function of spatial variable \mathbf{x} . Using the identities in equations (4.9), (4.10) and (4.11), the first order sensitivities of these parameters can be calculated. To start, the formulation for base state sensitivity of interaction index n ;

$$\frac{\partial \omega}{\partial n} = -\frac{\mathbf{p}^{\dagger H} \frac{\delta \mathbf{L}(\omega)}{\delta n} \mathbf{p}}{\mathbf{p}^{\dagger H} \frac{\partial \mathbf{L}(\omega)}{\partial \omega} |_{\omega} \mathbf{p}} \quad (4.12a)$$

$$\frac{\delta \mathbf{L}(\omega)}{\delta n} = -\frac{\dot{Q}_t}{U_b \rho(\mathbf{x}_r)} (\gamma - 1) e^{i\omega \tau} \int_{\Omega} \phi_k dV \nabla \phi_j(\mathbf{x}_r) \cdot \mathbf{n}_r \quad (4.12b)$$

For base state sensitivity of time delay τ ;

$$\frac{\partial \omega}{\partial \tau} = - \frac{\mathbf{p}^{\dagger H} \frac{\delta \mathbf{L}(\omega)}{\delta \tau} \mathbf{p}}{\mathbf{p}^{\dagger H} \frac{\partial \mathbf{L}(\omega)}{\partial \omega} |_{\omega} \mathbf{p}} \quad (4.13a)$$

$$\frac{\delta \mathbf{L}(\omega)}{\delta \tau} = -i\omega \frac{\dot{Q}_t}{U_b \rho(\mathbf{x}_r)} (\gamma - 1) n e^{i\omega\tau} \int_{\Omega} \phi_k dV \nabla \phi_j(\mathbf{x}_r) \cdot \mathbf{n}_r \quad (4.13b)$$

For base state sensitivity of speed of sound $\bar{c}(\mathbf{x})$,

$$\frac{\partial \omega}{\partial \bar{c}} = - \frac{\mathbf{p}^{\dagger H} \frac{\delta \mathbf{L}(\omega)}{\delta \bar{c}} \mathbf{p}}{\mathbf{p}^{\dagger H} \frac{\partial \mathbf{L}(\omega)}{\partial \omega} |_{\omega} \mathbf{p}} \quad (4.14a)$$

$$\begin{aligned} \frac{\delta \mathbf{L}(\omega)}{\delta \bar{c}} = & - \int_{\Omega} 2\bar{c} \nabla \phi_j \cdot \nabla \phi_k d\mathbf{x} \\ & - \frac{\dot{Q}_t}{U_b} \left(\frac{2\bar{c}(\mathbf{x}_r)}{p_{amb}} \right) \frac{\gamma - 1}{\gamma} n e^{i\omega\tau} \int_{\Omega} \phi_k dV \nabla \phi_j(\mathbf{x}_r) \cdot \mathbf{n}_r \end{aligned} \quad (4.14b)$$

4.3 Shape State Sensitivities

In thermoacoustic eigenvalue problem, the effect of small geometrical changes on growth rate of the complex eigenvalue is crucial information for optimizing combustor geometry. To ensure that the modified geometry is thermoacoustically stable, derived Helmholtz equation is solved for modified physical domain Ω_t which consists of deformable boundaries σ_t . These modifications are possible by concept of shape derivatives. In this section, shape derivatives for thermoacoustic eigenvalue problem is presented subjecting to various boundary conditions. The main reference of this section is [25].

4.3.1 Basic Shape Calculus

Reference [26] is useful guidance to introduce shape calculus. The spatial domain is mapped via $T_t : (t, x) \rightarrow T_t(x)$ using parameter t . If perturbed domain is defined as;

$$\Omega_t := T_t(\Omega)$$

the mapping operator $T_t(\Omega)$ can be defined using perturbation of identity;

$$T_t(\Omega) = (\mathbf{I} + t\mathbf{V})x = x + tV(x)$$

where \mathbf{I} is identity operator and \mathbf{V} is displacement operator. The general representation of the gradient of the shape functional \mathcal{J} is;

$$d\mathcal{J}(\Omega)[V] := \lim_{t \rightarrow 0} \frac{\mathcal{J}(\Omega_t) - \mathcal{J}(\Omega)}{t}$$

If \mathcal{J} is differentiable for all directions \mathbf{V} , then Hadamard form of this gradient can be written;

$$d\mathcal{J}(\Omega)[V] = \int_{\Gamma} (\mathbf{V} \cdot \mathbf{n}) g \, d\sigma \quad (4.15)$$

where g is called costate, shape gradient in this case. Right-hand side of the equation (4.15) contains terms that might not be written in Hadamard form. In order to get these forms, tangential gradient and divergence relations are practical;

$$\nabla_{\Gamma} f = \nabla f - \frac{\partial f}{\partial n} \mathbf{n} \quad (4.16a)$$

$$\nabla_{\Gamma} \cdot \mathbf{v} = \nabla \cdot \mathbf{v} - (\mathbf{D}\mathbf{v}\mathbf{n}) \cdot \mathbf{n} \quad (4.16b)$$

where f is a function $f \in C^2(\Omega, \mathbb{R})$, \mathbf{v} is a differentiable vector field, $\mathbf{D}\mathbf{v}$ is Jacobian of \mathbf{v} and \mathbf{n} is the outward unit normal vector.

Therefore, Tangential Stokes formula can be defined;

$$\int_{\Gamma} f \nabla_{\Gamma} \cdot \mathbf{v} + \nabla_{\Gamma} f \cdot \mathbf{v} \, d\sigma = \int_{\Gamma} \kappa f \mathbf{v} \cdot \mathbf{n} \, d\sigma \quad (4.17)$$

where $\kappa = \nabla_{\Gamma} \cdot \mathbf{v}$ is curvature of the boundary, which is zero for straight edges.

4.3.2 Shape Derivative for Boundary Condition

The shape gradient information of eigenvalue ω can be derived based on basic shape calculus formulae. The abstract formula will be obtained by taking Robin boundary condition into account since it includes Dirichlet and Neumann boundary conditions as a special cases. If the boundary Γ is decomposed into deformable (Γ_1) and non-deformable (Γ_0) parts, the thermoacoustic problem is redefined as;

$$\mathcal{L}(\omega)\hat{p} = 0 \quad \text{in } \Omega \quad (4.18a)$$

$$\frac{\partial \hat{p}}{\partial n} - \frac{i\omega}{\bar{c}Z} \hat{p} = 0 \quad \text{on } \Gamma = \Gamma_0 + \Gamma_1 \quad (4.18b)$$

The material and local shape derivatives for perturbed solution of eigenfunction \hat{p}_t are;

$$d\hat{p}[\mathbf{V}](x) = \left. \frac{d}{dt} \right|_{t=0} \hat{p}_t(x_t) \quad (4.19a)$$

$$\hat{p}'[\mathbf{V}](x) = \left. \frac{d}{dt} \right|_{t=0} \hat{p}_t(x) \quad (4.19b)$$

The combination of equations in (4.19) by applying chain rule;

$$d\hat{p}[\mathbf{V}] = \hat{p}'[\mathbf{V}] + \mathbf{V} \cdot \nabla \hat{p} \quad (4.20)$$

This material derivative is zero for any boundary condition. Using the expression of (4.20), the material shape derivative for Robin boundary condition relation (4.18b) becomes;

$$\nabla \hat{p}' \cdot \mathbf{n} + \nabla \hat{p} \cdot \mathbf{n}' + \mathbf{V} \cdot \nabla (\nabla \hat{p} \cdot \mathbf{n}) = \frac{i\omega'}{\bar{c}Z} \hat{p} + \frac{i\omega}{\bar{c}Z} \hat{p}' - \frac{i\omega}{\bar{c}^2 Z} \mathbf{V} \cdot \nabla \bar{c} \hat{p} + \frac{i\omega}{\bar{c}Z} \mathbf{V} \cdot \nabla \hat{p} \quad (4.21)$$

If $\mathbf{V} = C\mathbf{n}$, the local shape derivative of \mathbf{n} becomes $\mathbf{n}' = d\mathbf{n}$ and

$$d\mathbf{n} = -\nabla_{\Gamma}(\mathbf{V} \cdot \mathbf{n}) = -\nabla_{\Gamma} C \implies \nabla \hat{p} \cdot \mathbf{n}' = -\nabla \hat{p} \cdot \nabla_{\Gamma} C \quad (4.22a)$$

$$\mathbf{V} \cdot \nabla (\nabla \hat{p} \cdot \mathbf{n}) = C \frac{\partial^2 \hat{p}}{\partial n^2} \quad (4.22b)$$

Therefore, equation (4.21) can be written as;

$$\frac{\partial \hat{p}}{\partial n} - \frac{i\omega}{\bar{c}Z} \hat{p}' = \nabla \hat{p} \cdot \nabla_{\Gamma} C - C \frac{\partial^2 \hat{p}}{\partial n^2} + \frac{i\omega'}{\bar{c}Z} \hat{p} - C \frac{i\omega}{\bar{c}^2 Z} \frac{\partial \bar{c}}{\partial n} \hat{p} + C \frac{i\omega}{\bar{c}Z} \frac{\partial \hat{p}}{\partial n} \quad \text{on } \Gamma_1 \quad (4.23)$$

4.3.3 Shape Derivatives for Eigenvalue

The general formula of shape derivative for any boundary condition is derived. This section describes the derivation of shape derivatives for eigenvalue in Hadamard form. To start, material shape derivatives of (4.18) yields;

$$\mathcal{L}'(\omega')\hat{p} + \mathcal{L}(\omega)\hat{p}' = 0 \quad \text{in } \Omega \quad (4.24a)$$

$$\frac{\partial \hat{p}'}{\partial n} - \frac{i\omega}{\bar{c}Z}\hat{p}' - \frac{i\omega'}{\bar{c}Z}\hat{p} = 0 \quad \text{on } \Gamma_0 \quad (4.24b)$$

$$\frac{\partial \hat{p}}{\partial n} - \frac{i\omega}{\bar{c}Z}\hat{p}' = \nabla \hat{p} \cdot \nabla_{\Gamma} C - C \frac{\partial^2 \hat{p}}{\partial n^2} + \frac{i\omega'}{\bar{c}Z}\hat{p} - C \frac{i\omega}{\bar{c}^2 Z} \frac{\partial \bar{c}}{\partial n} \hat{p} + C \frac{i\omega}{\bar{c}Z} \frac{\partial \hat{p}}{\partial n} \quad \text{on } \Gamma_1 \quad (4.24c)$$

The premultiplication of (4.24a) with complex conjugate of adjoint eigenvector $\hat{p}^{\dagger*}$ and integration over the domain Ω gives;

$$\langle \hat{p}^{\dagger} | \mathcal{L}'(\omega')\hat{p} \rangle \omega' + \langle \mathcal{L}^{\dagger}(\omega^*)\hat{p}^{\dagger} | \hat{p}' \rangle + \int_{\Gamma} \hat{p}^{\dagger*} \bar{c}^2 \frac{\partial \hat{p}'}{\partial n} dS - \int_{\Gamma} \hat{p}' \bar{c}^2 \frac{\partial \hat{p}^{\dagger*}}{\partial n} dS = 0 \quad (4.25)$$

Integration by parts operation on \mathcal{L} produces boundary terms. In addition, adjoint definition of the same problem is;

$$\mathcal{L}^{\dagger}(\omega^*)\hat{p}^{\dagger} = 0 \quad \text{in } \Omega \quad (4.26a)$$

$$\frac{\partial \hat{p}^{\dagger}}{\partial n} - \frac{i\omega}{\bar{c}Z}\hat{p}^{\dagger} = 0 \quad \text{on } \Gamma \quad (4.26b)$$

With the help of (4.26a), second term of (4.25) is zero. The terms that contain ω' and \hat{p}' can be grouped or eliminated, if necessary. Equations in (4.24) and (4.26) are utilized to obtain shape derivative relation for eigenvalue;

$$\underbrace{\left(\langle \hat{p}^{\dagger} | \mathcal{L}'(\omega')\hat{p} \rangle + \int_{\Gamma} \hat{p}^{\dagger*} \frac{i\bar{c}}{Z} \hat{p} dS \right)}_{\text{Equals to 1}} \omega' + \int_{\Gamma_1} \hat{p}^{\dagger*} \bar{c}^2 \left(\nabla \hat{p} \cdot \nabla_{\Gamma} C - C \frac{\partial^2 \hat{p}}{\partial n^2} + C \frac{i\omega}{\bar{c}^2 Z} \frac{\partial \bar{c}}{\partial n} \hat{p} + C \frac{i\omega}{\bar{c}Z} \frac{\partial \hat{p}}{\partial n} \right) dS = 0 \quad (4.27)$$

The relation in front of the eigenvalue shape derivative ω' is imposed as normalization relation of adjoint eigenvector. Also eigenvalue (ω) terms in (4.27) can be removed using (4.18b) and (4.26b) and ω' is given as;

$$\omega' = \int_{\Gamma_1} -\hat{p}^{\dagger*} \bar{c}^2 \nabla \hat{p} \cdot \nabla_{\Gamma} C + C \hat{p}^{\dagger*} \bar{c}^2 \frac{\partial^2 \hat{p}}{\partial n^2} + C \hat{p}^{\dagger*} \bar{c} \frac{\partial \bar{c}}{\partial n} \frac{\partial \bar{p}}{\partial n} - C \frac{\partial \hat{p}^{\dagger*}}{\partial n} \bar{c}^2 \frac{\partial \hat{p}}{\partial n} dS \quad (4.28)$$

The term $\hat{p}^{\dagger*} \bar{c}^2 \nabla \hat{p} \cdot \nabla_{\Gamma} C$ is not in Hadamard form, so tangential Stokes formula (4.17) can be applied;

$$-\hat{p}^{\dagger*} \bar{c}^2 \nabla \hat{p} \cdot \nabla_{\Gamma} C = -\kappa C \hat{p}^{\dagger*} \bar{c}^2 \underbrace{\nabla \hat{p} \cdot \mathbf{n}}_{\frac{\partial \hat{p}}{\partial n}} + C \nabla_{\Gamma} \cdot (\hat{p}^{\dagger*} \bar{c}^2 \nabla \hat{p}) \quad (4.29)$$

Considering definition of tangential divergence (4.16b), the second term in (4.29) can be given as;

$$\nabla_{\Gamma} \cdot (\hat{p}^{\dagger*} \bar{c}^2 \nabla \hat{p}) = \nabla \cdot (\hat{p}^{\dagger*} \bar{c}^2 \nabla \hat{p}) - \left((\mathbf{n} \cdot \nabla) (\hat{p}^{\dagger*} \bar{c}^2 \nabla \hat{p}) \right) \cdot \mathbf{n} \quad (4.30a)$$

$$= \nabla \cdot (\hat{p}^{\dagger*} \bar{c}^2 \nabla \hat{p}) - \frac{\partial \hat{p}^{\dagger*}}{\partial n} \bar{c}^2 \frac{\partial \hat{p}}{\partial n} - 2 \hat{p}^{\dagger*} \bar{c} \frac{\partial \bar{c}}{\partial n} \frac{\partial \hat{p}}{\partial n} - \hat{p}^{\dagger*} \bar{c}^2 \frac{\partial^2 \hat{p}}{\partial n^2} \quad (4.30b)$$

Inserting equation (4.30) into equation (4.28) gives main equation for shape derivative of the eigenvalue;

$$\omega' = \int_{\Gamma_1} C \left(-\hat{p}^{\dagger*} \left(\kappa \bar{c}^2 + \bar{c} \frac{\partial \bar{c}}{\partial n} \right) \frac{\partial \hat{p}}{\partial n} + \nabla \cdot (\hat{p}^{\dagger*} \bar{c}^2 \nabla \hat{p}) - 2 \frac{\partial \bar{p}^{\dagger*}}{\partial n} \bar{c}^2 \frac{\partial \hat{p}}{\partial n} \right) dS \quad (4.31)$$

This final equation holds the shape derivative of eigenvalue for Robin boundary condition. As mentioned before, the relations for Dirichlet and Neumann boundary conditions can be extracted from (4.31). For Dirichlet boundaries, \hat{p} and \hat{p}^{\dagger} are zero. Therefore, equation (4.31) becomes;

$$\omega' = \int_{\Gamma_1} C \left(\nabla \cdot (\hat{p}^{\dagger*} \bar{c}^2 \nabla \hat{p}) - 2 \frac{\partial \bar{p}^{\dagger*}}{\partial n} \bar{c}^2 \frac{\partial \hat{p}}{\partial n} \right) dS \quad (4.32a)$$

$$\omega' = \int_{\Gamma_1} C \left(\nabla \hat{p}^{\dagger*} \bar{c}^2 \nabla \hat{p} + \underbrace{\hat{p}^{\dagger*} \bar{c}^2 \nabla^2 \hat{p}}_0 - 2 \frac{\partial \bar{p}^{\dagger*}}{\partial n} \bar{c}^2 \frac{\partial \hat{p}}{\partial n} \right) dS \quad (4.32b)$$

$$\omega' = \int_{\Gamma_1} C \left(\frac{\partial \bar{p}^{\dagger*}}{\partial n} \bar{c}^2 \frac{\partial \hat{p}}{\partial n} - 2 \frac{\partial \bar{p}^{\dagger*}}{\partial n} \bar{c}^2 \frac{\partial \hat{p}}{\partial n} \right) dS = - \int_{\Gamma_1} C \left(\frac{\partial \bar{p}^{\dagger*}}{\partial n} \bar{c}^2 \frac{\partial \hat{p}}{\partial n} \right) dS \quad (4.32c)$$

For Neumann boundary condition, the normal gradients $\partial\hat{p}/\partial n$ and $\partial\bar{p}^\dagger/\partial n$ are zero. If \hat{q} is zero, equation (2.19) implies $\nabla \cdot (\bar{c}^2 \nabla \hat{p}) = -\omega^2 \hat{p}$, then shape derivative of Neumann boundary reads;

$$\omega' = \int_{\Gamma_1} C \left(\nabla \cdot (\hat{p}^{\dagger*} \bar{c}^2 \nabla \hat{p}) \right) dS \quad (4.33a)$$

$$\omega' = \int_{\Gamma_1} C \left(\nabla \hat{p}^{\dagger*} \cdot (\bar{c}^2 \nabla \hat{p}) + \hat{p}^{\dagger*} \cdot \nabla (\bar{c}^2 \nabla \hat{p}) \right) dS \quad (4.33b)$$

$$\omega' = \int_{\Gamma_1} C \left(\bar{c}^2 \nabla \hat{p}^{\dagger*} \cdot \nabla \hat{p} - \omega^2 \hat{p}^{\dagger*} \hat{p} \right) dS \quad (4.33c)$$

4.4 Taylor Remainder Test

In order to check the accuracy of gradients found via adjoint method, the Taylor test is elegant tool to verify adjoint calculations.

The derived shape gradient formulae can be tested with respect to any control point \mathbf{x} on any boundary. It is obvious to expect that the gradient calculated via adjoint $f_a(\mathbf{x})$ should be very close to the gradient calculated via finite difference $f_d(\mathbf{x})$.

If the new control point is defined as $\mathbf{x}_1 = \mathbf{x}_0 + \Delta\mathbf{x}$, the Taylor series of the function f ;

$$f(\mathbf{x}_1) = f(\mathbf{x}_0) + \underbrace{\frac{df}{dx} \Big|_{\mathbf{x}=\mathbf{x}_0}}_{f_d(\mathbf{x}_0)} (\mathbf{x}_1 - \mathbf{x}_0) + \mathcal{O}((\mathbf{x}_1 - \mathbf{x}_0)^2) \quad (4.34)$$

Then difference between finite difference and adjoint calculations is formulated as;

$$\delta f = [f(\mathbf{x}_0) + f_d(\mathbf{x}_0)(\Delta\mathbf{x}) + \mathcal{O}((\Delta\mathbf{x})^2)] - [(f(\mathbf{x}_0) + f_a(\mathbf{x}_0)(\Delta\mathbf{x})] \quad (4.35a)$$

$$\delta f = [f_d(\mathbf{x}_0) - f_a(\mathbf{x}_0)] \Delta\mathbf{x} + \mathcal{O}((\Delta\mathbf{x})^2) \quad (4.35b)$$

In case the gradients are calculated correctly via adjoint and $\Delta\mathbf{x}$ is sufficiently small, the term in the brackets should converge to zero. Hence, the second order term gains dominance and the function Δf should demonstrate parabolic behaviour for different $\Delta\mathbf{x}$ values. If the behaviour of Δf is linear, it points out that there is a bug in adjoint code.

Chapter 5

Results

In this section, eigenvalue and shape derivative calculations of dolfin and dolfinx codes are presented for Rijke Tube. Additionally, eigenmodes and shape derivatives of different configurations for MICCA combustor and realistic gas turbine combustor are also presented using dolfin code.

5.1 Rijke Tube

It is worth to mention that the most canonical example to illustrate thermoacoustic instability is Rijke tube. Because of the nature of its simplicity, Rijke tube serves broad physical insight into thermoacoustic phenomena [27]. Hence, thermoacoustic models can be build for Rijke tube first, then they can be extended to complex geometries.

This tube has one electrical heat source which placed at x_f from one end. With the powered heat source, base air flow occurs through the tube due to the natural convection. As a test case, one dimensional and two dimensional configurations are considered. All the physical properties of the flow variables are assumed to be constant in the radial direction.

The system parameters has been taken from [7] which is tabulated in Table 5.1. The nondimensionalized mean density distribution $\bar{\rho}$ is modeled as;

$$\bar{\rho}(\mathbf{x}) = \rho_u + \frac{\rho_d - \rho_u}{2} \left[1 + \tanh \left(\frac{\mathbf{x} - \mathbf{x}_f}{a_f} \right) \right] \quad (5.1)$$

where subscripts u and d denotes upstream and downstream considering the flame location x_f , then a_f is the flame region width. Therefore, the speed of sound distribution can be defined with the equation $\bar{c} = \sqrt{\gamma p_a / \bar{\rho}}$.

Table 5.1 Dimensional and non-dimensional parameters of modelled Rijke Tube [7]

Parameter	Dimensional		Non-dimensional
	value	unit	value
L	1	m	1
d	0.047	m	0.047
r	287	$\text{Jkg}^{-1}\text{K}^{-1}$	287
γ	1.4	-	1.4
P_a	100000	Pa	100000
ρ_a	1.22	kg m^{-3}	1.22
ρ_i	1.22	kg m^{-3}	1.4
ρ_d	0.85	kg m^{-3}	0.975
c_u	338.75	m s^{-1}	1
c_d	405.83	m s^{-1}	1.198
R_u	-0.975-0.05i	-	-0.975-0.05i
R_d	-0.975-0.05i	-	-0.975-0.05i
Q	200	W	200
U_b	0.1	m s^{-1}	0.1
N	0.014	-	0.014
τ	0.0015	s	0.0015
n	28	J m^{-1}	0.1613
x_f	0.25	m	0.25
a_f	0.025	-	0.025
x_r	0.2	m	0.2

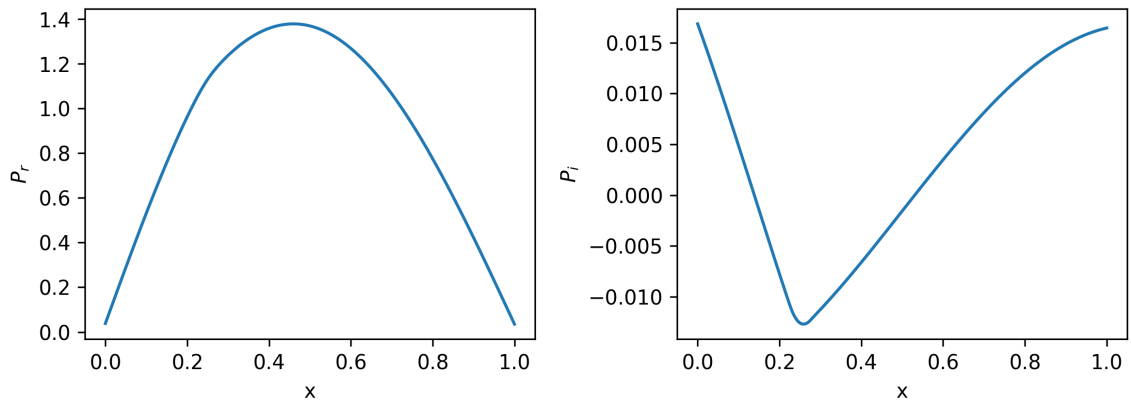
5.1.1 Eigenmodes

The normalization of direct eigenfunctions is defined such that

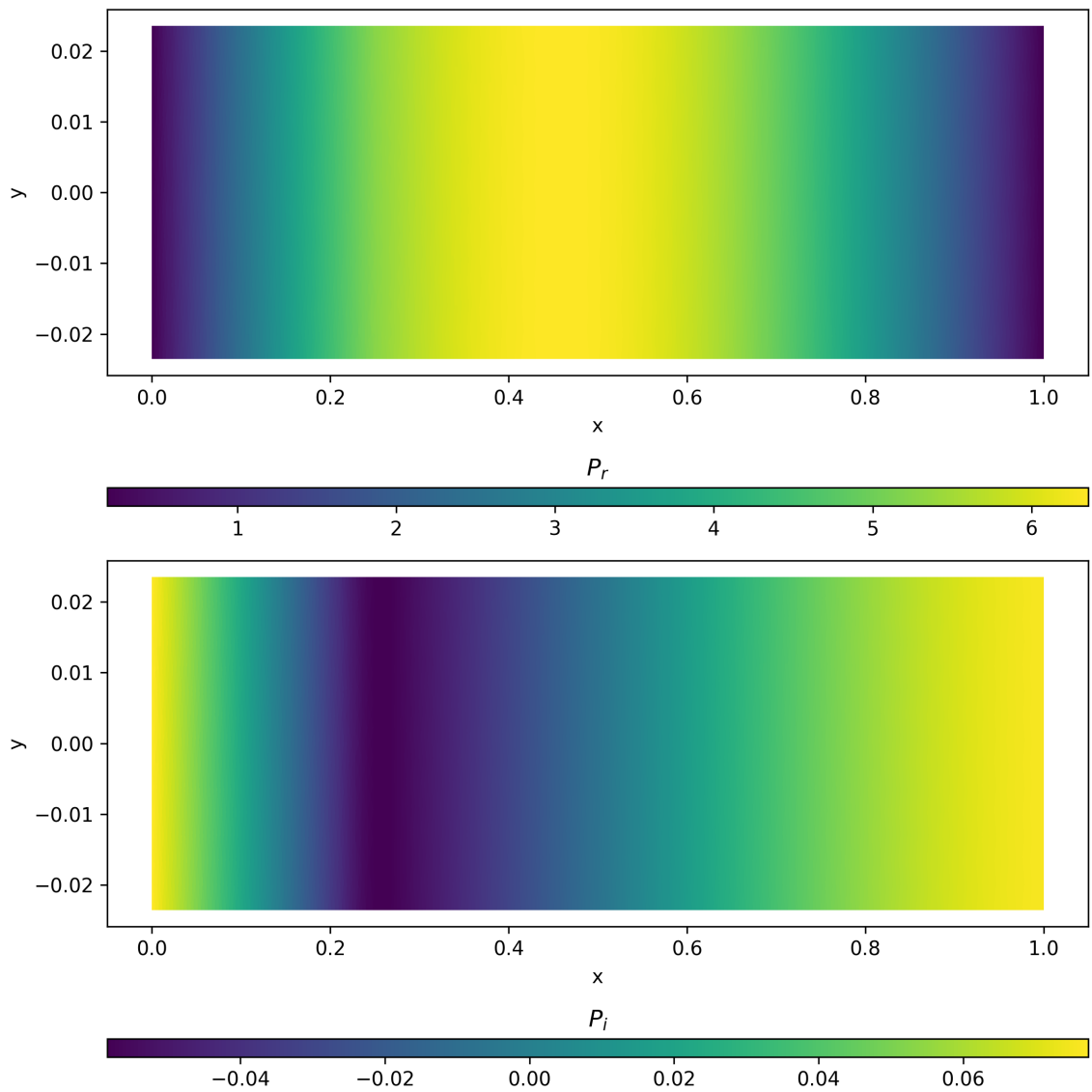
$$\int_{\Omega} \hat{p} \hat{p} dV = 1$$

Boundary conditions at the inlet and outlet are considered as Robin boundary condition which represents the most realistic physical state for acoustic waves. The acoustic impedance $Z = (1 + \Gamma)/(1 - \Gamma)$ is imposed at both ends of the tube by taking reflection coefficients into account according to Table 5.1. In addition to Robin boundaries in one dimensional case, the Neumann boundaries for bottom and top walls are considered in two dimensional case.

Eigenmodes of the Rijke Tube are shown in Figure 5.1 and Figure 5.2 for Dolfin and Dolfinx code. In these plots, every left subplots shows the real part and every right subplot shows imaginary part of the eigenvectors.

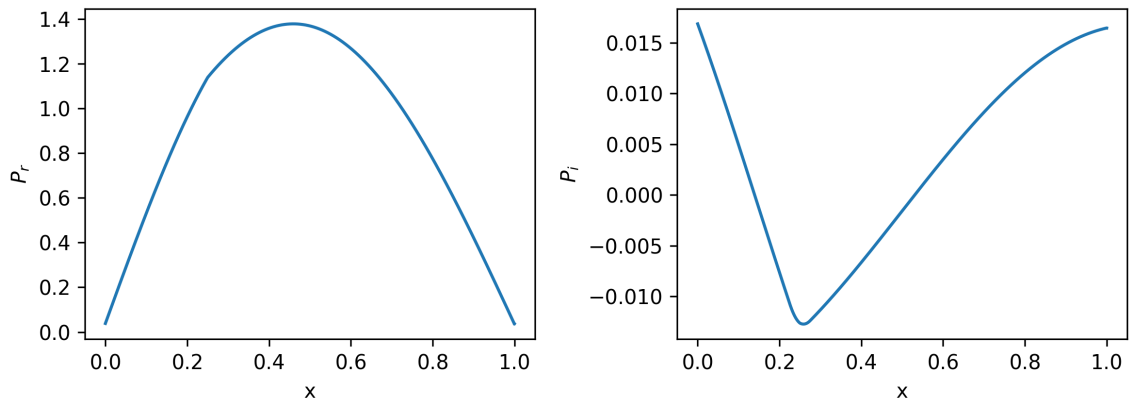


(a) One Dimensional

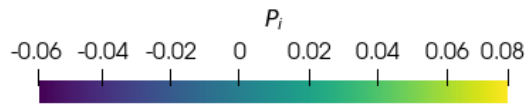
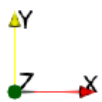
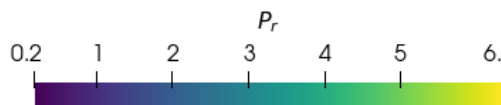


(b) Two Dimensional Planar

Fig. 5.1 Eigenmodes of Rijke Tube in Dolfin Code [28]



(a) One Dimensional



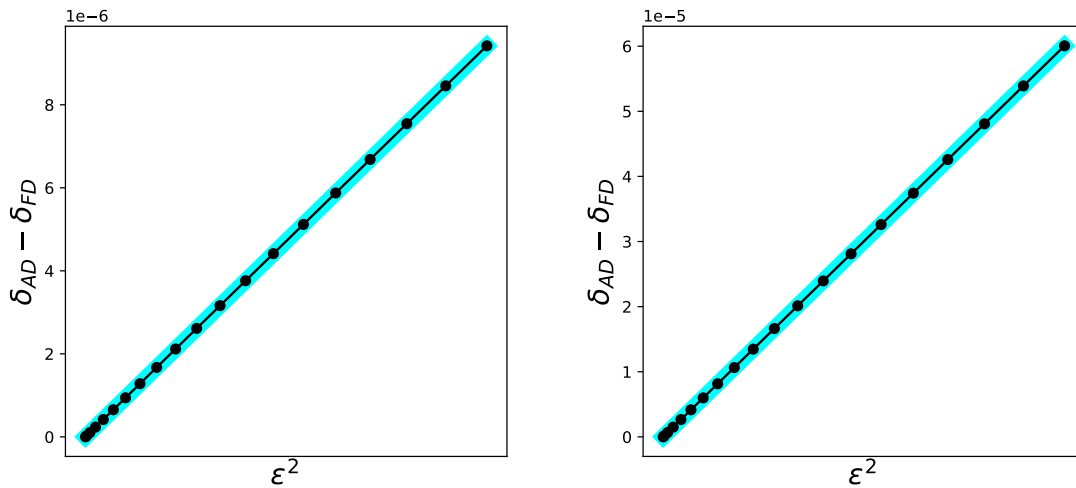
(b) Two Dimensional Planar

Fig. 5.2 Eigenmodes of Rijke Tube in Dolfinx Code

Dolfin code is previously implemented in [25]. Non-dimensional variables are used for eigenvalue calculations of Rijke tube. Two dimensional cases in Dolfin and Dolfinx codes have same eigenvalues around $\omega \approx +3.4254 + 0.0019i$. The calculated eigenvectors are also in good agreement according to the comparison between Figure 5.1 and Figure 5.2.

5.1.2 Base State Sensitivities

The sensitivities of base state parameters are given in section §4.2. Therefore sensitivity of the eigenvalue (ω) with respect to interaction index (n) is found $\partial n/\partial \omega = -0.02299 + 0.17881i$. Similarly, sensitivity for time delay (τ) is calculated as $\partial n/\partial \tau = -0.09884 - 0.01276i$. In order to check validities of adjoint calculations, Taylor tests are made;



(a) Sensitivity for Interaction index (n)

(b) Sensitivity for Time Delay (τ)

Figure 5.3a and Figure 5.3b show parabolic characteristic with squared x-axis variables. Consequently, the implemented adjoint code passes Taylor remainder test for calculations of interaction index and time delay sensitivities.

5.1.3 Shape Optimization

Shape optimization of the Rijke tube is presented in this section. The optimization domain is treated as two dimensional planar case. 13 BSpline control points are defined for upper and lower boundaries which account for Neumann boundary condition. The polynomial degree of the basis functions specified as 2 to enable quadratic BSplines. System parameters are remained as in Table 5.1.

Shape Derivatives for Control Points

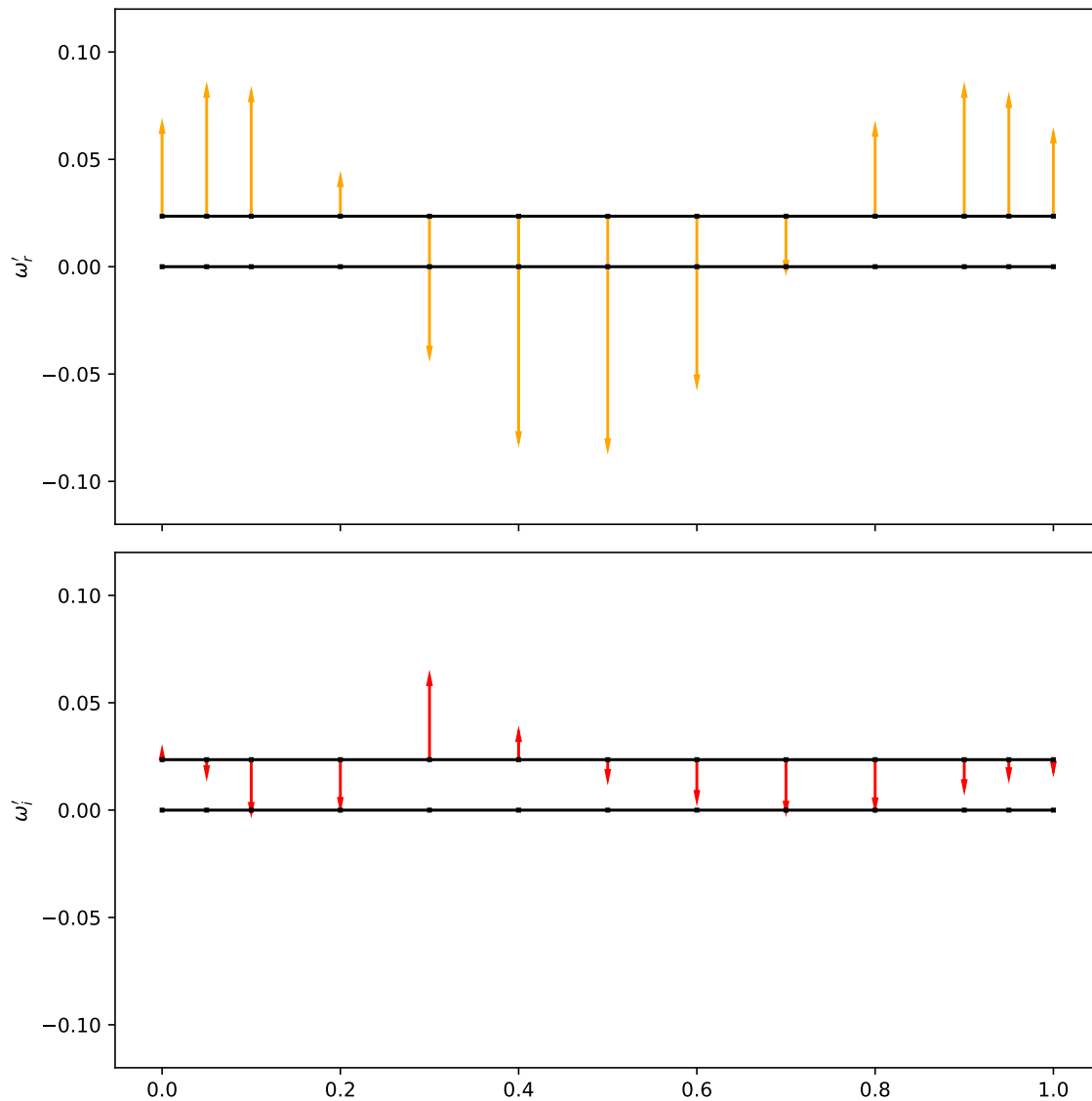


Fig. 5.4 Shape Derivatives (ω') of each control point for Rijke Tube in Dolfin [17]

Equation (4.33) is considered for calculating shape derivatives for each control point along Neumann boundaries. Calculated derivatives are complex numbers including frequency and growth rate components for both x and y directions. It is clear to expect that shape derivatives in x direction becomes zero due to the rectangular computation domain. The calculated derivatives for y direction is represented in Figure 5.4 and 5.5 for both Dolfin and Dolfinx.

Vector representation is useful to monitor magnitudes of the frequency and growth rate components of the derivatives, then each derivative is scaled with some arbitrary scalar for visualization. The upper plots shows the frequency portion while the lower plots accounts for growth rate of the derivative values.

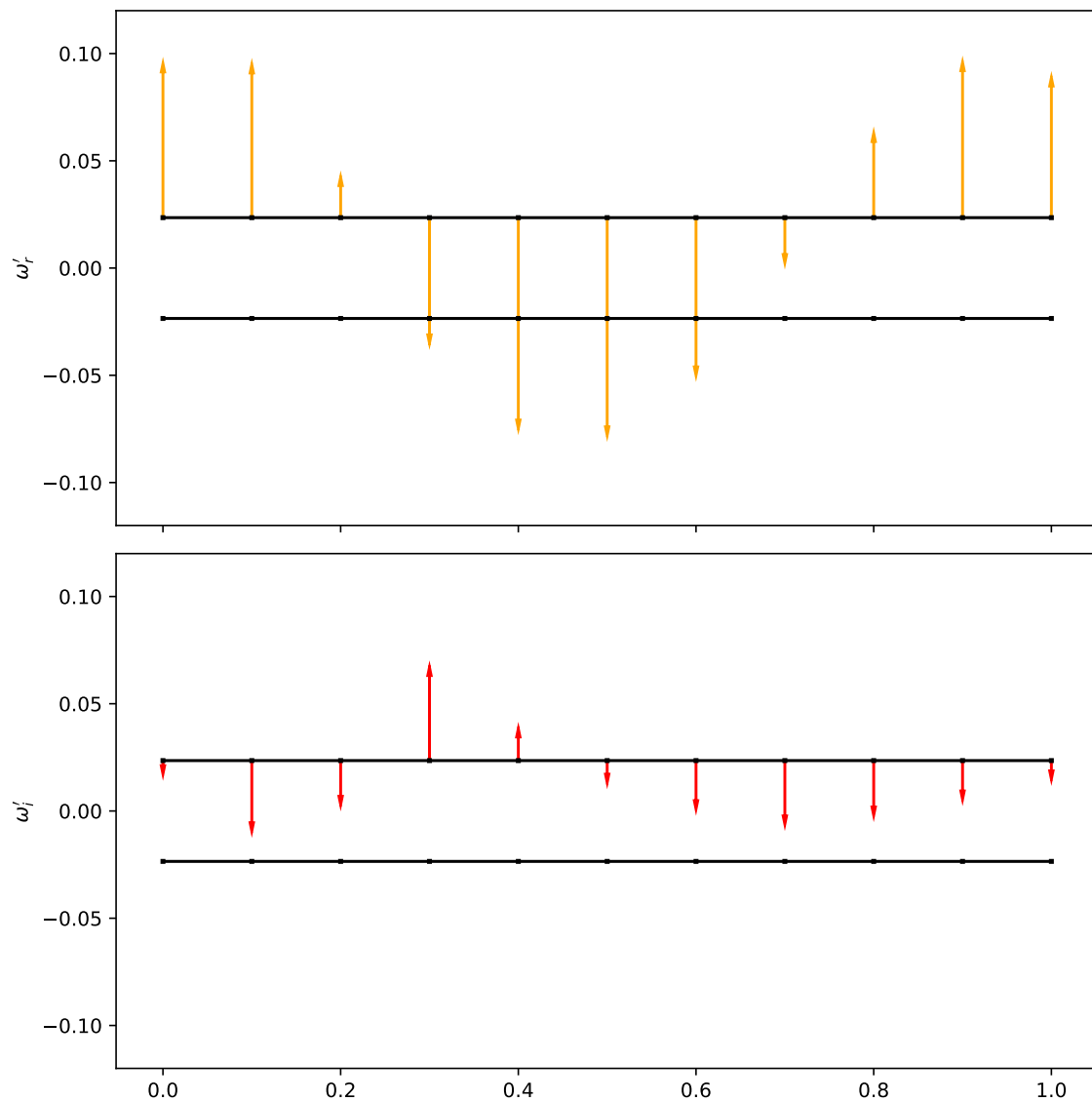


Fig. 5.5 Shape Derivatives (ω') of each control point for Rijke Tube in Dolfinx

Optimized Shape

In order to optimize the shape thermoacoustically, the lower plot in Figure 5.4 should be taken into consideration, since the aim is reducing the growth rate. The vectors pointing

+y direction indicates that if the control point moved in +y direction, then growth rate is expected to be increased. Therefore, the control points are moved in contrast to direction of shape derivative vectors.

During shape optimization, arbitrary step size Δy can be chosen and points can be relocated at each iteration. Next, the eigenvalue and eigenmode of the new geometry is determined. If the growth rate is still positive, then new shape derivatives can be calculated for new control points again. After a few iterations, the final geometrical domain is appeared as in Figure 5.6. While the eigenvalue of the initial geometry is $3.42738+0.00180i$, the eigenvalue of optimized Rijke tube becomes $3.56103-0.00776i$ with wavy boundaries.

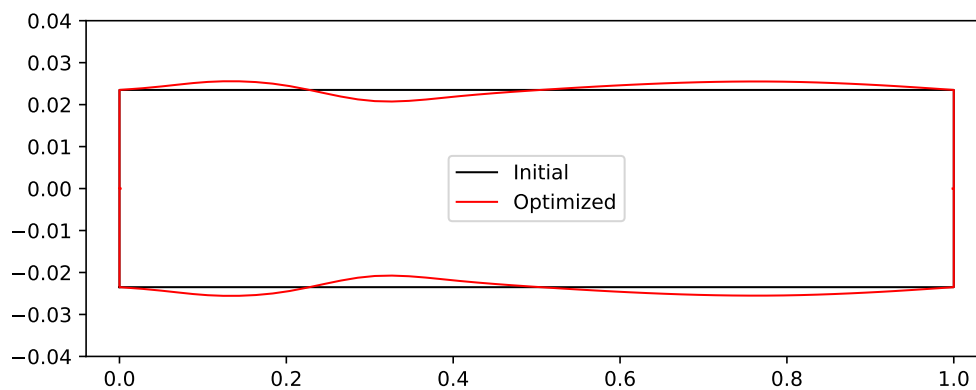


Fig. 5.6 Optimized geometry of Rijke Tube [17]

5.2 MICCA Combustor

To observe the thermoacoustic instabilities in laboratory scale, rigorous investigations have been performed in annular combustor called MICCA. It has been designed in order to resemble all features of gas turbine combustors, by having plenum, burner, injector and combustion chamber (Figure 5.7).

In this section, implemented solver with Dolfin is used for calculating eigenmodes and shape derivatives of certain configurations of MICCA combustor. For first case, geometrical specifications are kept same as in [8]. Table 5.2 also provides additional parameters for numerical simulations. The local speed of sound is computed from the temperature distribution using $\bar{c} = \sqrt{kRT}$.

Table 5.2 Dimensional parameters of Micca combustor

Parameter	Dimensional	
	value	unit
r	287	$\text{Jkg}^{-1}\text{K}^{-1}$
γ	1.4	-
P_a	101325	Pa
T_a	300	K
T_u	300	K
T_d	$1521-321(z/l_{cc})^2$	K
Q	2080	W
U_b	0.66	m s^{-1}
z_f	0.0	m
x_r	-0.02	m

As explained in section §2.3, the flame transfer function should be defined as analytical form in order to being differentiable. The analytical form of flame transfer function is approximated using state-space representation [29];

$$\frac{d}{dt}\mathbf{x} = \mathbf{S}_1\mathbf{x} + \mathbf{S}_2u' \quad (5.2)$$

$$\dot{q}' = \mathbf{S}_3\mathbf{x} + \mathbf{S}_4u' \quad (5.3)$$

where \mathbf{x} is state vector and system matrices $\mathbf{S}_1, \mathbf{S}_2, \mathbf{S}_3$ and \mathbf{S}_4 are taken from reference [11].

The Laplace transform ($s = i\omega$) of (5.2) and (5.3) with relative substitutions gives;

$$\text{FTF}(\omega) = \frac{\hat{q}}{\hat{u}} = (\mathbf{S}_3(i\omega\mathbf{I} - \mathbf{S}_1)^{-1}\mathbf{S}_2 + \mathbf{S}_4)$$

$$\frac{\partial^k}{\partial^k \omega} \text{FTF}(\omega) = \left((-i)^k k! \mathbf{S}_3 (i\omega\mathbf{I} - \mathbf{S}_1)^{-(k+1)} \mathbf{S}_2 \right) \text{ for } k \geq 1$$

Equation (5.2) is enabling the differentiability of flame transfer function by using experimental data and that is crucial for applying perturbation theory[29].

For shape optimization, due to existence of repeated eigenvalues, degenerate eigenmodes \hat{p} and \hat{p}^\dagger are used to calculate eigenvalue problem [17];

$$\left(\int CG(\hat{p}_i^\dagger, \hat{p}_j) dS \right) = 0 \quad (5.4)$$

Direct and adjoint eigenfunctions are normalized such that $\int_{\Omega} \hat{p} \hat{p} dV = 1$. Eigenvalues of (5.4) gives shape derivative ω' for azimuthal modes. $C = 1/A$ where A denotes the surface area. In this way, local average of the shape derivatives is obtained for corresponding boundary faces. Three different configurations of MICCA combustor are proposed; base case, extended plenum case and extended plenum with cooling holes case.

5.2.1 Micca - Base Case

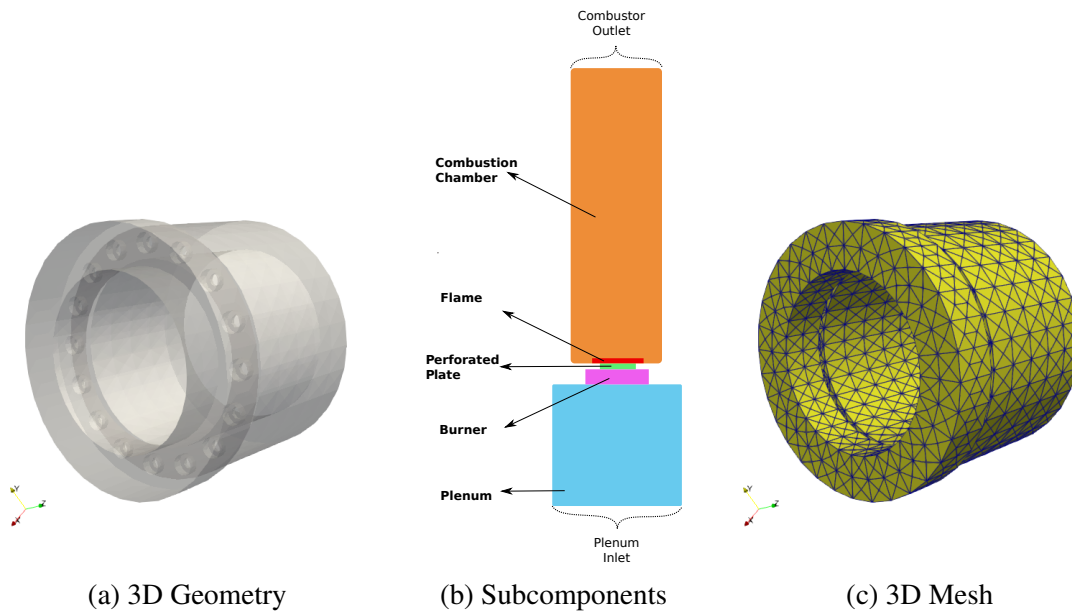


Fig. 5.7 Geometry of Micca Combustor

Eigenmodes

The geometry, boundaries and mesh of base case for MICCA combustor visualized in 5.7. For eigenvalue calculations, all the boundaries are modelled as Neumann boundary condition apart from Dirichlet boundary for combustion chamber outlet (Figure 5.7b). End correction is added to the combustion chamber's outlet end since the pressure node occurs at short distance to the combustor outlet boundary [11].

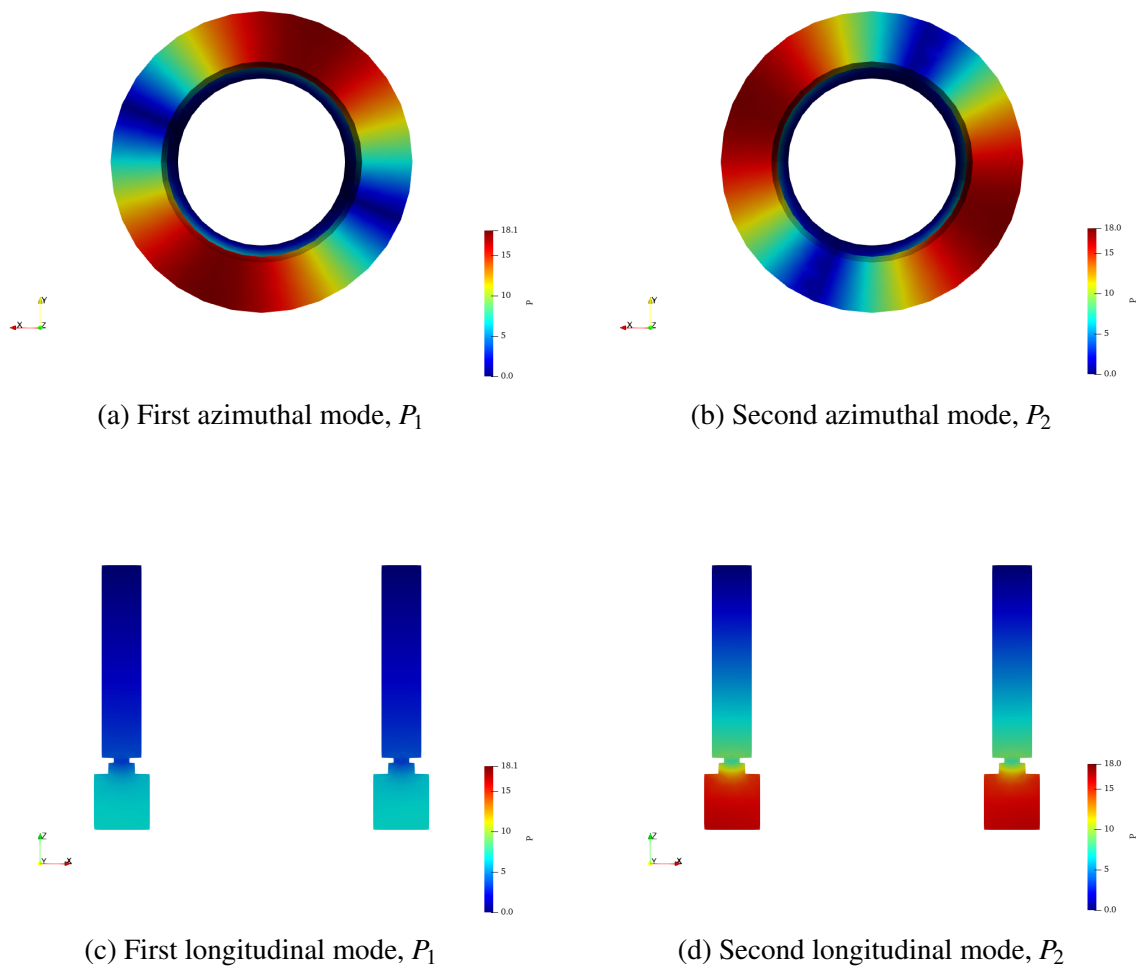


Fig. 5.8 Eigenmodes of Micca Combustor

Calculated azimuthal degenerate eigenmodes are displayed in Figure 5.8. Eigenfrequencies of the first (Figure 5.8a) and second (Figure 5.8b) azimuthal eigenmode are found as $\omega_1 = 507.7682 + 83.6084i$ and $\omega_2 = 507.7638 + 83.6773i$. As expected, they have very close eigenfrequencies while having different mode shapes.

Intersection planes pointing normal Y direction demonstrate longitudinal modes of azimuthal modes. These longitudinal modes display quarter-wave standing modes in longitudinal direction (Figure 5.8c and Figure 5.8d). Finally, phase shift between azimuthal modes is plotted in Figure 5.9. Circular data has been extracted from plenum section of the MICCA. Acoustic waves show 90° phase angle difference.

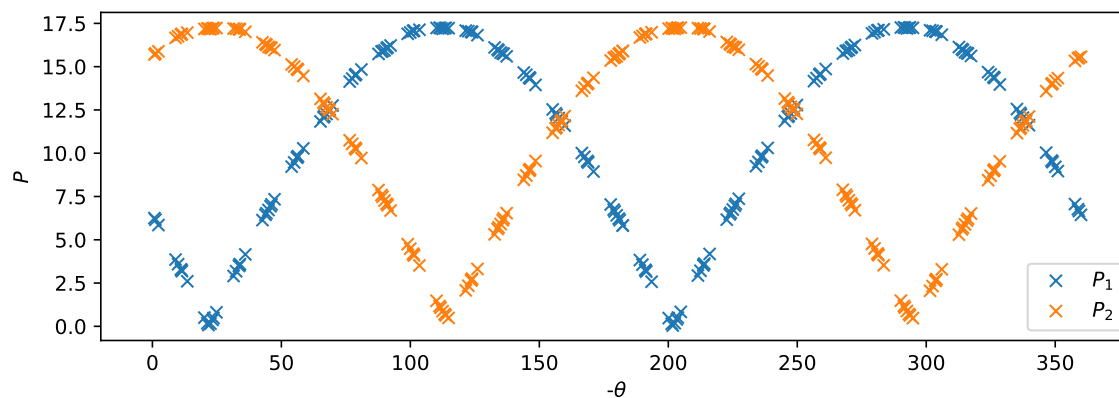


Fig. 5.9 Phase shift between P_1 and P_2

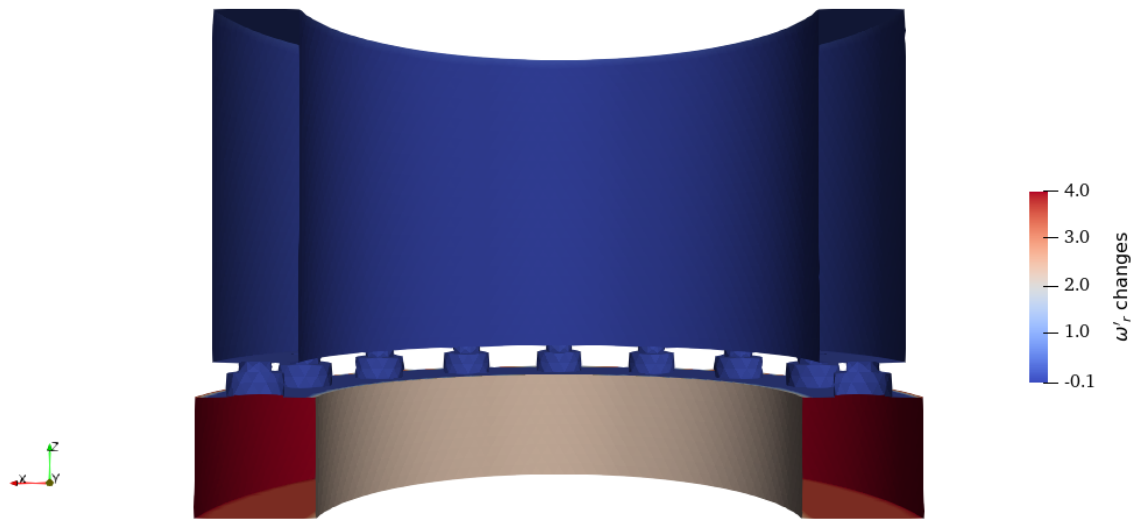
Shape Derivatives

During shape optimization study, geometries of burner and injector are fixed. Since they play significant roles for combustion process in chamber, any geometrical change on their shapes might effect the combustion performance.

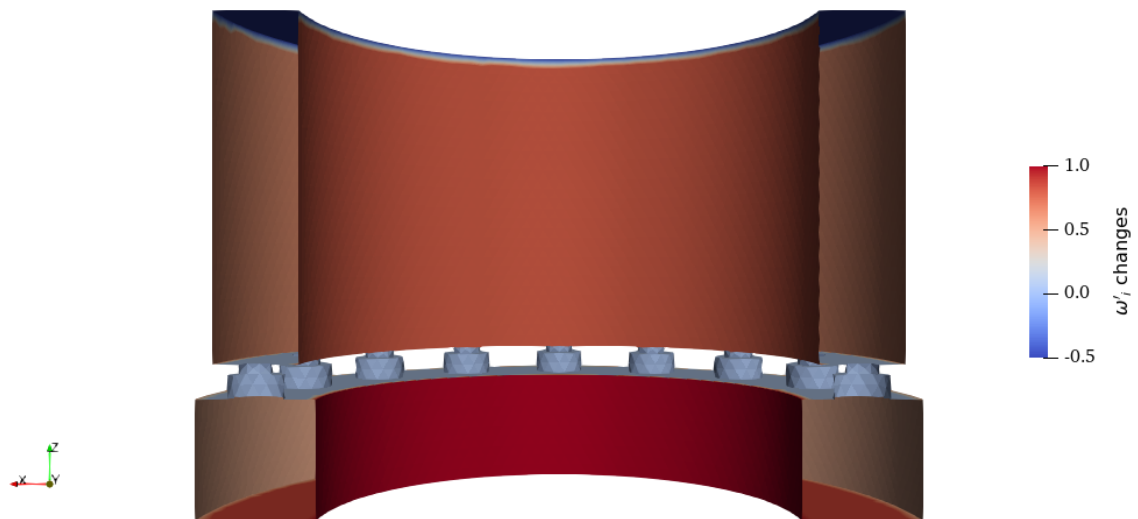
As introduced in start of this section, (5.4) is used to calculate shape derivatives of boundaries. Using calculated eigenmodes for direct and adjoint methods, average shape derivative for each boundary is plotted in Figure 5.10.

Sensitivities in Figure 5.10a shows that geometrical changes on plenum has significant effect on eigenfrequency of the system. All the plenum boundaries can be moved outwards to reduce frequency component of eigenvalue. Geometry of combustion has negligible effect on frequency. Shape derivatives for combustion chamber surfaces are relatively small comparing to the plenum surfaces.

For thermoacoustic stabilization, shape derivatives in Figure 5.10b can be elaborated. Geometries of plenum and combustion chamber has significant effect on growth rate of the system. Most sensitive boundary is inner boundary of plenum. The scaled shape derivatives suggest that all 3 surfaces of plenum can be moved outwards and inner and outer boundaries of combustion chamber could be moved outwards. Only boundary that can be moved inwards is the combustion chamber outlet to reduce growth rate of the MICCA combustor.



(a) Shape sensitivity of eigenvalue for changes in frequency



(b) Shape sensitivity of eigenvalue for changes in growth rate

Fig. 5.10 Shape derivatives for MICCA - base case

5.2.2 Micca - Extended Plenum

New configuration is proposed to resemble realistic gas turbine combustor which has an extended plenum surrounding combustion chamber (Figure 5.11b). For this case, boundaries of plenum outlet and combustor outlet are specified as Dirichlet boundaries. Rest of the boundaries are kept as Neumann boundaries. Similar to base case of MICCA, end correction is considered again for combustion chamber's outlet and plenum's outlet.

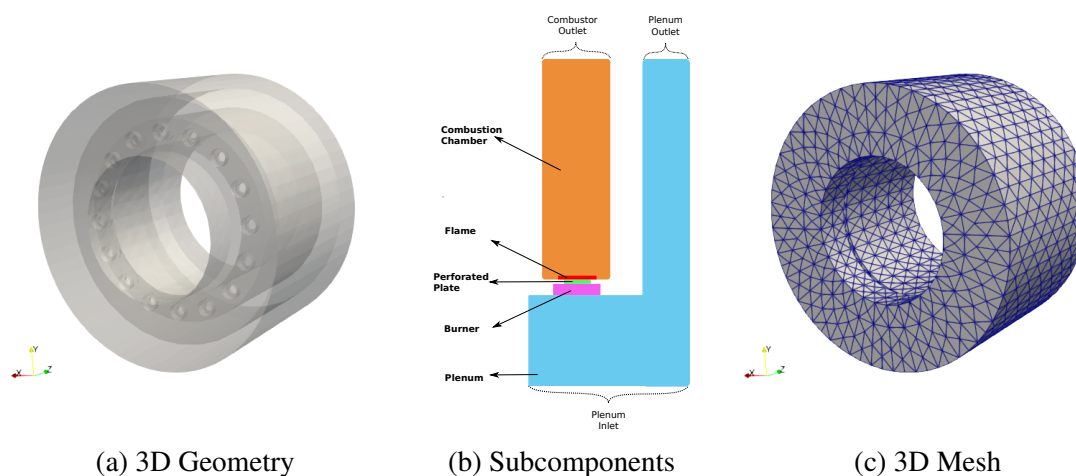


Fig. 5.11 Geometry of Micca Combustor - extended plenum case

Eigenmodes

Azimuthal eigenmodes for extended plenum case are shown in Figure 5.12. Eigenfrequencies of the first (Figure 5.12a) and second (Figure 5.12b) azimuthal eigenmode are found as $\omega_1 = 516.7917 + 45.0086$ and $\omega_2 = 516.8010 + 45.00087i$. They have very close eigenfrequencies with reduced growth rate comparing to original MICCA.

Section views of the eigenmodes on XZ plane are displayed in Figure 5.12c and Figure 5.12d. Similar to base case, longitudinal eigenmodes are captured in +Z direction. Furthermore, thermoacoustic characteristics of extended part of the plenum and combustion chamber are similar in magnitude of acoustic pressure.

Shape Derivatives

Shape derivatives for extended plenum case are calculated and plotted in Figure 5.13. Geometries of burner and injector kept same again. All the derivatives are scaled for better visualization.

The effect of shape derivatives on frequency of the system shown in Figure 5.13a. Similar to base case, most influential part is plenum. The changes on plenum inlet boundary has most considerable impact on frequency. In addition, inner and outlet boundaries of plenum can be moved outwards to reduce frequency. Surface movement through outward for inner and outer walls of combustion chamber and outer surface of plenum is increases the frequency of the system, since they have negative shape derivatives.

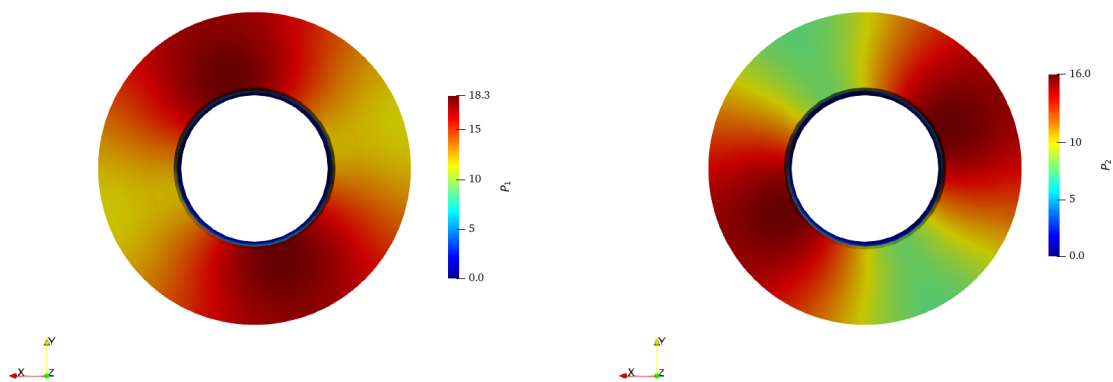
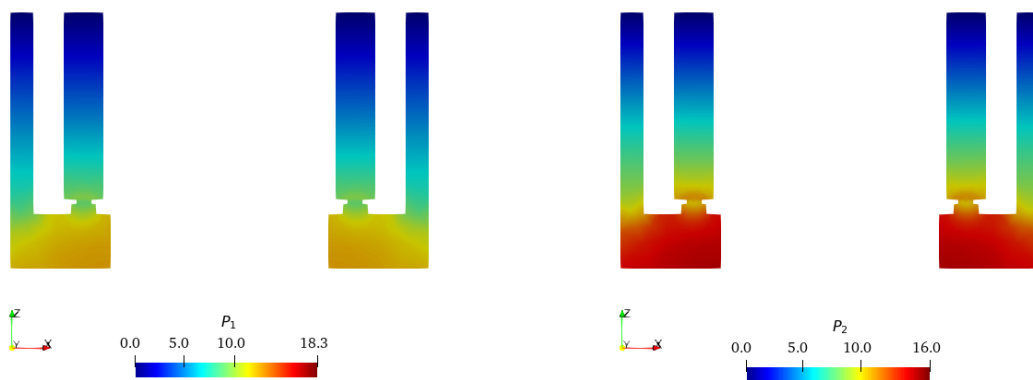
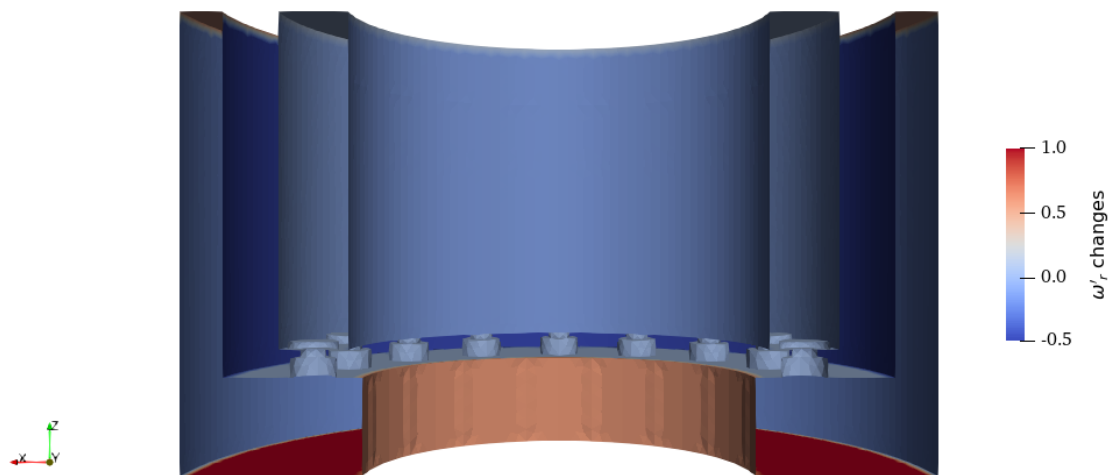
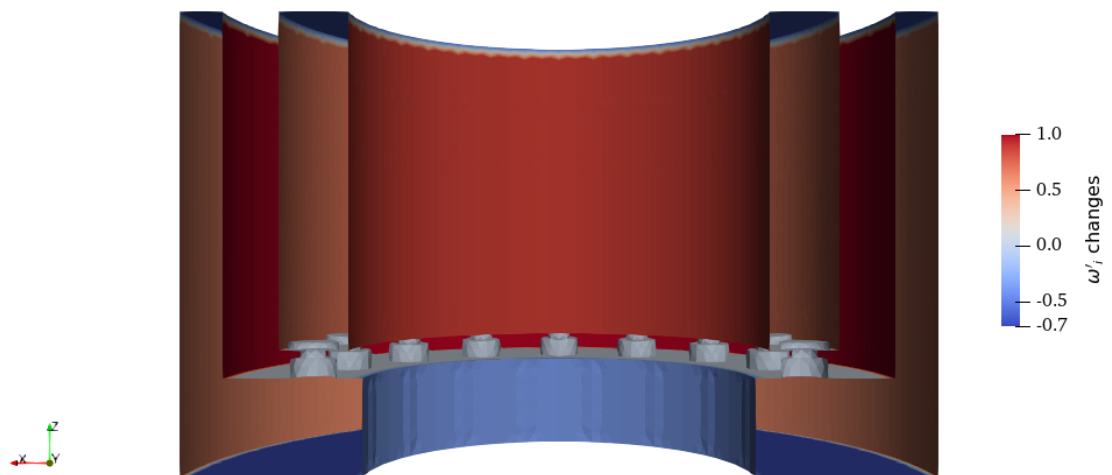
(a) First azimuthal mode, P_1 (b) Second azimuthal mode, P_2 (c) First longitudinal mode, P_1 (d) Second longitudinal mode, P_2

Fig. 5.12 Eigenmodes of Micca Combustor - extended plenum case

In order to reduce growth rate, inner and inlet surfaces of plenum and outlet faces of plenum and combustion chamber can be moved inwards. Moreover, in addition to inner and outer faces of combustion chamber, outer and inner surface of extended section could be moved in direction of their normal vectors to improve growth rate of the system.



(a) Sensitivity of eigenvalue for changes in frequency



(b) Sensitivity of eigenvalue for changes in growth rate

Fig. 5.13 Shape derivatives for MICCA - extended plenum case

5.2.3 Micca - Extended Plenum with Cooling Holes

Last configuration for MICCA combustor includes cooling holes between combustion chamber and extended plenum (Figure 5.14). Similar to previous cases, Dirichlet boundary condition imposed on boundaries of plenum outlet and combustor outlet while other boundaries are specified as Neumann boundaries. Number of cooling holes between plenum and combustion chamber is 16, each cooling hole has 15mm radius and distance to flame is 175mm.

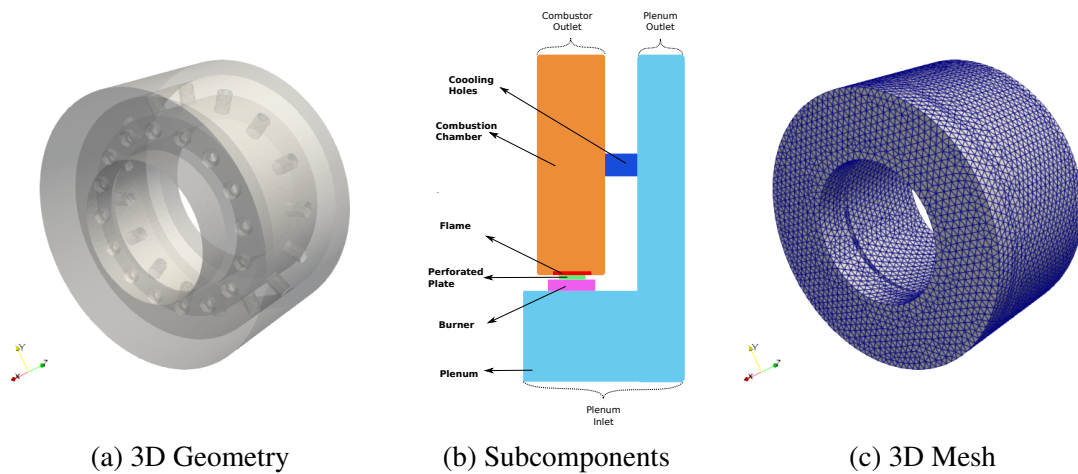


Fig. 5.14 Geometry of Micca Combustor with cooling holes

Eigenmodes

Azimuthal eigenmodes are calculated for MICCA with cooling holes and plotted in Figure 5.15. The first azimuthal mode has eigenfrequency of $\omega_1 = +535.2372 + 53.6872i$ and second azimuthal mode has eigenfrequency of $\omega_2 = +533.6472 + 54.5960i$. It can be clearly seen that eigenmodes are identical in magnitude but the phase angle difference between eigenmodes is 90° . Adding cooling holes with extended plenum decreased growth rate of the eigenvalues comparing to MICCA - base case. However, adding cooling holes is increased growth rate comparing to MICCA - extended plenum case. The total surface area is increased with cooling holes to dissipate acoustic energy, but phase angle relationship between heat release rate fluctuation and acoustic wave might lead to improve system's instability according to the Rayleigh criterion (1.1).

Additionally, longitudinal thermoacoustic eigenmodes in +Z direction can be seen in Figure 5.15c and Figure 5.15d for both azimuthal modes in XZ plane section view.

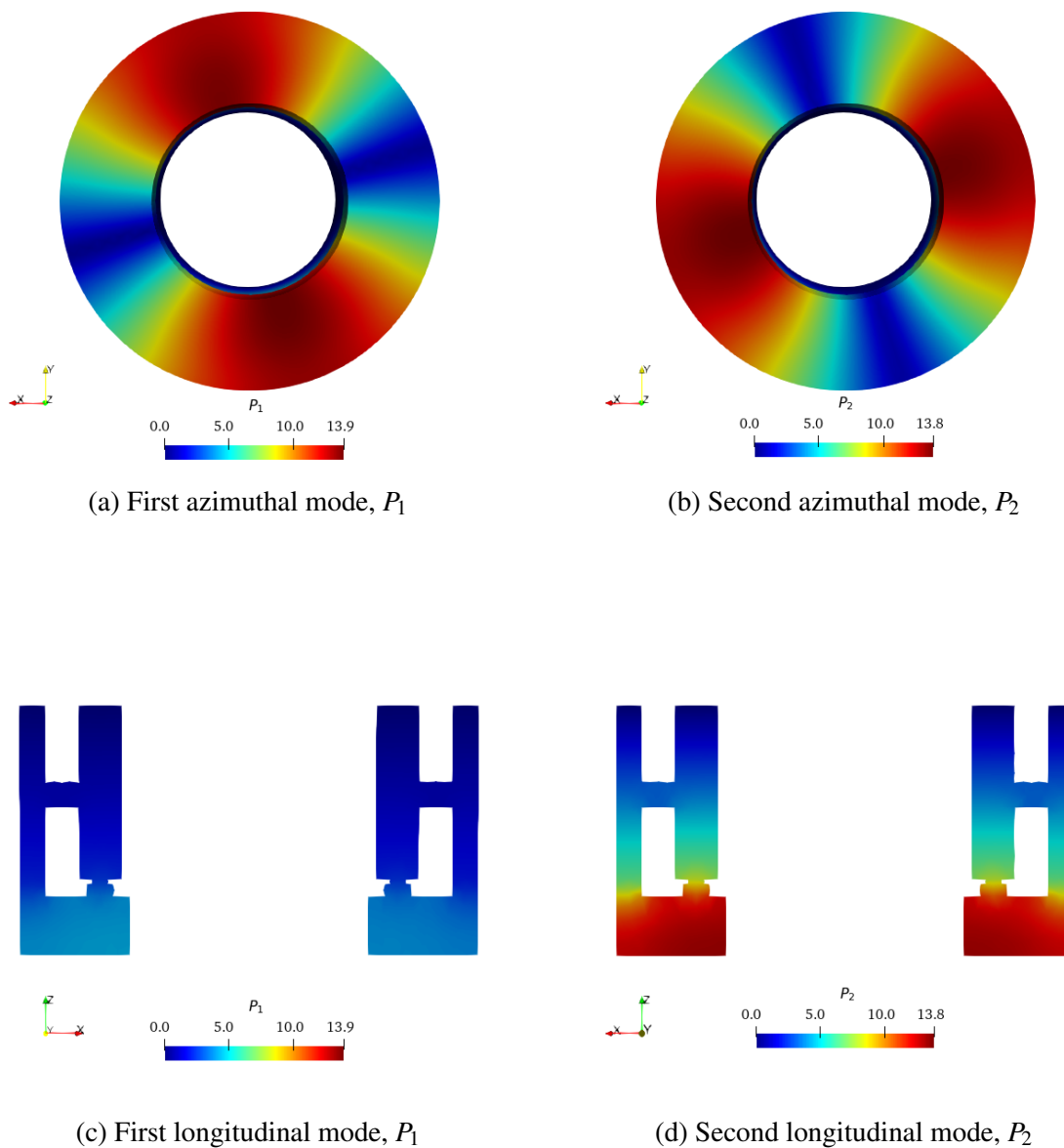
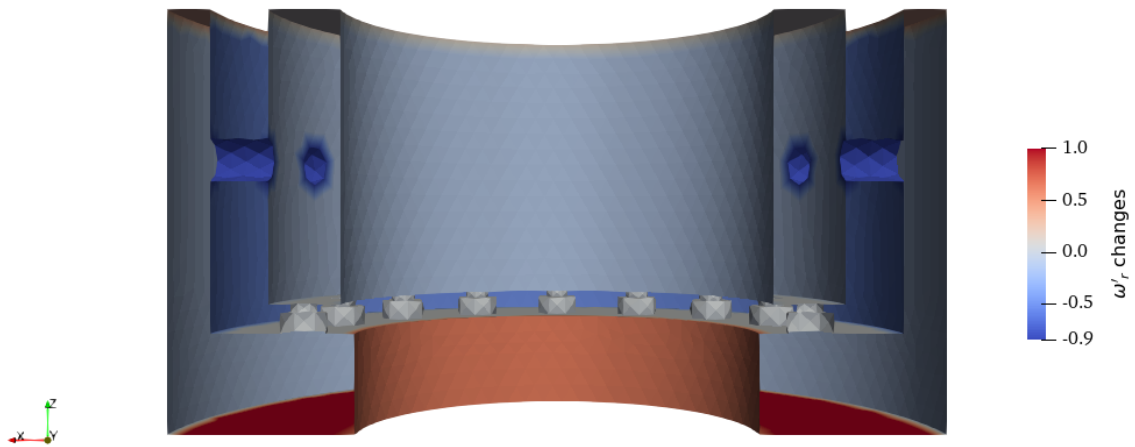


Fig. 5.15 Eigenmodes of Micca Combustor - extended plenum with cooling holes

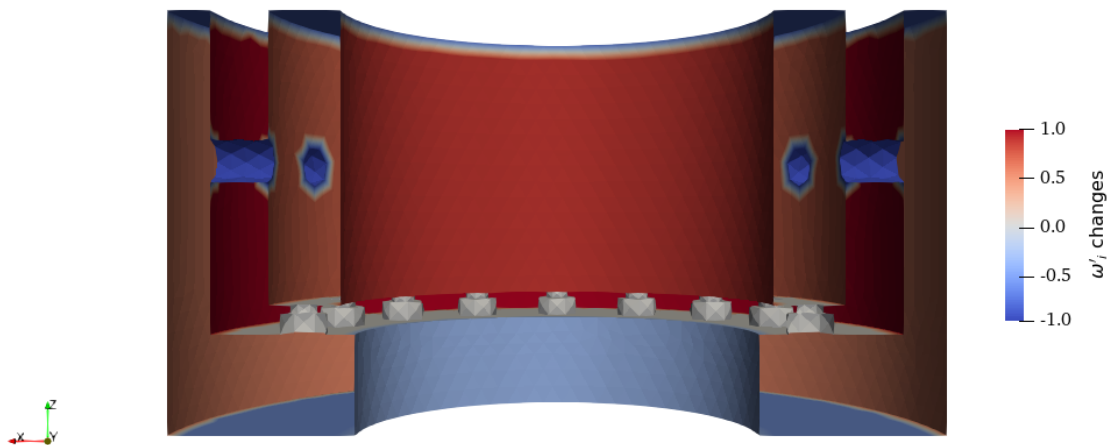
Shape Derivatives

Figure 5.16 shows shape sensitivities of all boundaries. Effect of cooling holes on frequency and growth rate of the eigenvalue is displayed in Figure 5.16a and Figure 5.16b. Similar to previous case, inner and inlet faces of plenum and outlet surfaces can be moved in surface normal direction to reduce frequency of the system,

Improvement in growth rate of the system can be achieved by moving boundaries of outer plenum, outer and inner surfaces of combustion chamber could be moved in normal vector directions. In contrast to shape derivative values for frequency, inner and inlet faces of plenum and outlet surfaces of the combustor can be moved inwards. Furthermore, radii of the cooling holes could be decreased to decrease growth rate.



(a) Sensitivity of eigenvalue for changes in frequency

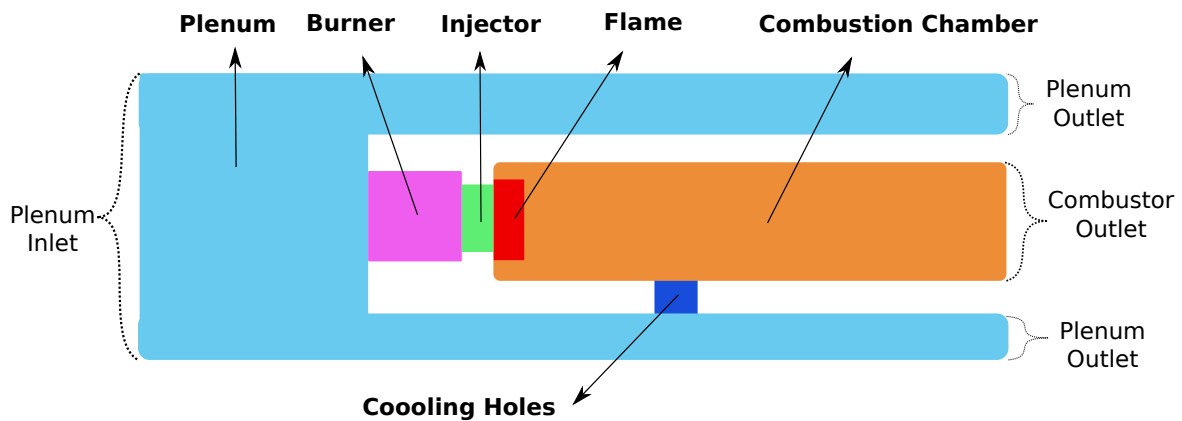


(b) Sensitivity of eigenvalue for changes in growth rate

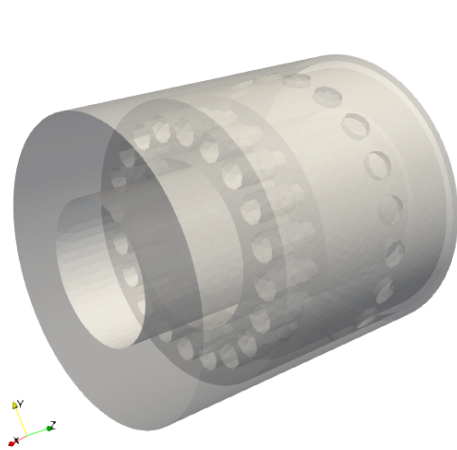
Fig. 5.16 Shape derivatives for MICCA - extended plenum with cooling holes

5.3 Realistic Combustor

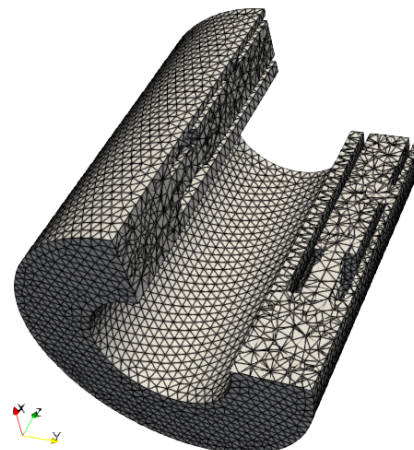
One of the aims of this study is optimizing real gas turbine combustor geometries thermoacoustically. As an initial step, the realistic combustor geometry is simplified further to reduce complexity during meshing process. Schematic diagram of proposed geometry is sketched in Figure 5.17a. Geometry generation accomplished by using open-source CAD environment FreeCAD [30]. Mesh generation of CAD geometry is performed by means of Gmsh. For this case, specified dimensions of the subcomponents feature realistic combustor geometry for typical gas turbine. 20 sector is considered with 20 cooling holes and 3D mesh of single sector is plotted in Figure 5.17c.



(a) Section view of proposed real combustor components



(b) 3D geometry



(c) 3D mesh and section view

Fig. 5.17 Real combustor geometry and mesh

For thermoacoustic eigenmode calculations, lot of simulation parameters are kept same as in MICCA combustor simulations. Only heat release rate per burner changed to 500kW and reference point location (x_r) is changed to (0,0,-0.08). Modelling of flame response is accomplished by $n - \tau$ model for $n = 1$ and $\tau = 0.003s$.

Eigenmodes

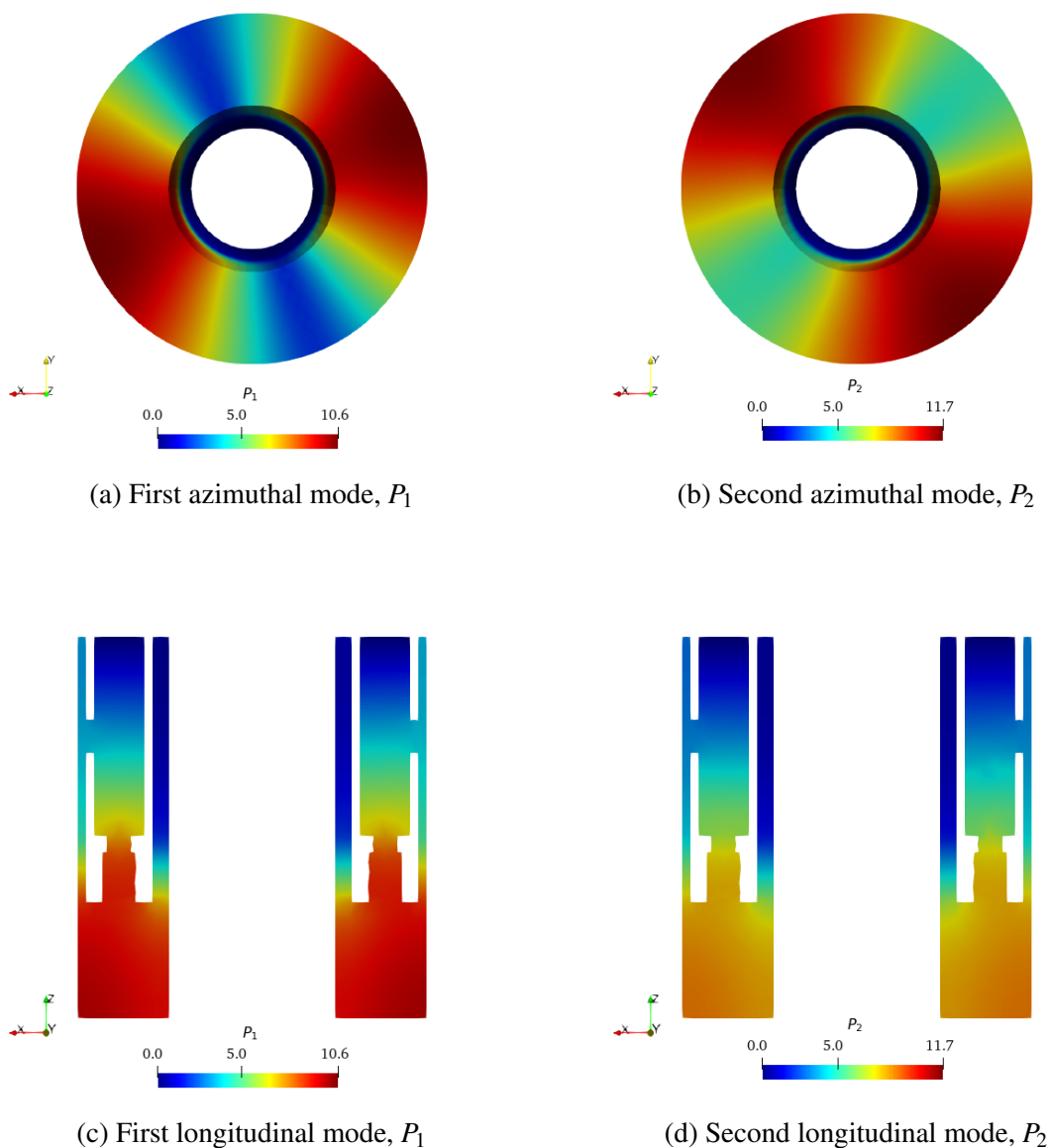


Fig. 5.18 Eigenmodes of realistic combustor

Azimuthal and longitudinal thermoacoustic modes of real combustor are captured and monitored in Figure 5.18. The computed eigenfrequencies for first and second azimuthal modes are $\omega_1 = +407.8497 + 0.2663i$ and $\omega_2 = +407.9930 + 0.2676i$ respectively. The 90° phase angle difference can be seen in Figure 5.18a and Figure 5.18b.

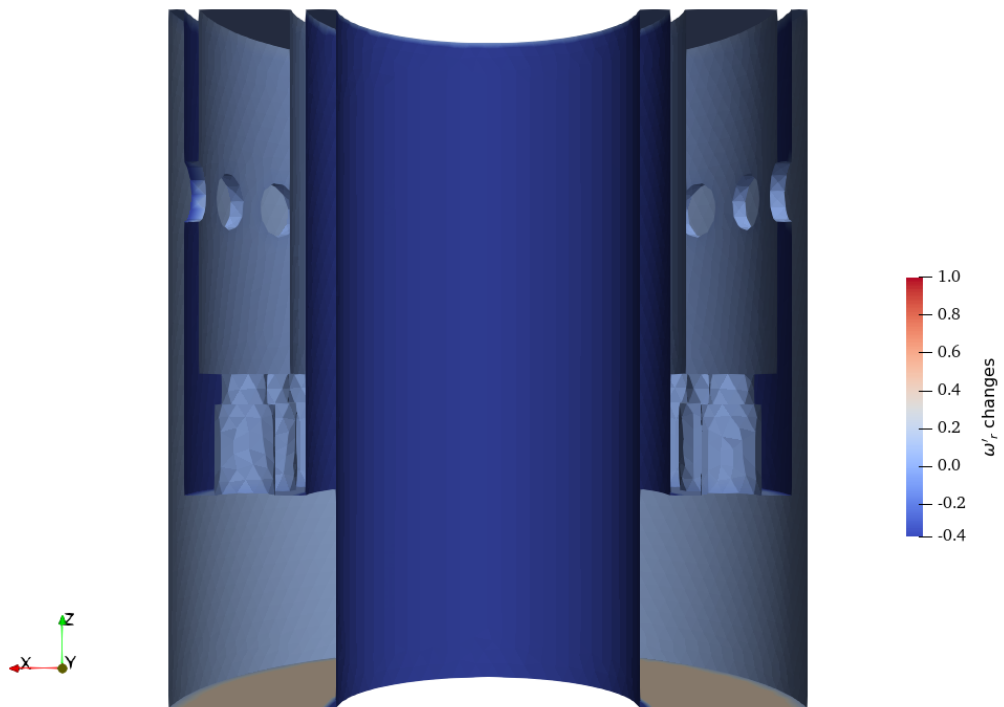
In addition to azimuthal eigenmodes, longitudinal eigenmodes are observed in +Z direction (Figure 5.18c and Figure 5.18d).

Shape Derivatives

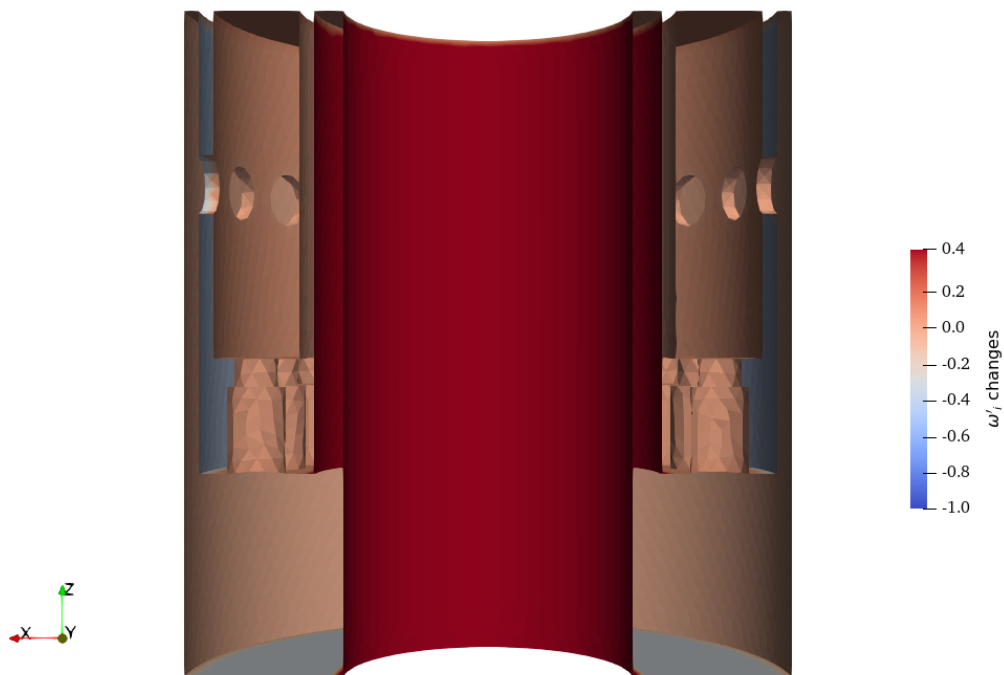
Shape derivatives for boundary faces are calculated except for boundaries of burner and injector. The most influential part is plenum for both components of the eigenfrequency.

Shape derivatives for frequency is visualized in Figure 5.19a. The negative valued boundary faces implies increment in frequency of the system, if they moved in normal vector direction for corresponding boundary face. Conversely, positive valued shape derivatives reduces the frequency if they moved outwards with respect to its boundary.

For thermoacoustic stabilization, Figure 5.19b shows the shape derivative values effecting growth rate of the system. Scaled shape derivatives suggest that positive valued boundaries could be moved in surface normal direction for lowering the growth rate. It can be also deduced that cooling holes have almost negligible effect on eigenvalue of the system.



(a) Sensitivity of eigenvalue for changes in frequency



(b) Sensitivity of eigenvalue for changes in growth rate

Fig. 5.19 Shape derivatives for realistic combustor

Chapter 6

Further Work

6.1 Current Findings

In this report, the methodology of shape optimization for a thermoacoustically unstable system has been presented. Derivation of non-homogeneous Helmholtz equation with frequency-dependent boundary conditions is given assuming zero Mach number mean flow. Finite element discretization is applied and obtained weak forms are implemented using open-source finite element frameworks Dolfin and Dolfinx [31, 32].

Horizontal Rijke tube and annular laboratory combustor MICCA are treated as benchmark cases. Additionally, different geometrical configurations for MICCA combustor and realistic gas turbine combustor are introduced. Flame response of the thermoacoustic system are modelled by $n - \tau$ formulation and state space approach using experimental data.

Longitudinal and azimuthal eigenmodes are successfully captured for each geometry using implemented solvers. For Rijke tube, base state sensitivities of interaction index n and time delay τ are calculated and checked using Taylor test. Results of Dolfin and Dolfinx are showed good agreement.

Starting by Rijke tube case, shape derivatives are calculated for different designs of MICCA combustor and realistic gas turbine combustor. Effect of boundary displacements on frequency and growth rate is presented for proposed geometries.

6.2 Future Work

- The shape parametrization of three dimensional geometries will be implemented.
- Effect of number and size of cooling holes will be investigated.

- More realistic geometries will be implemented such as gas turbine combustor. Shape optimization will be done for reducing the growth rate of the combustor.
- Developed solver uses $n - \tau$ formulation or experimental data for modelling flame response. More robust models for flame transfer function will be discussed.
- Current solver tested for only Rijke tube and MICCA combustor. More challenging benchmark cases will be implemented.
- Parallelization of code is essential for more complex and bigger geometries. Code is tested for 1,2,3 and 4 number of cores. Parallel runs with more than 4 processes will be performed.
- Complete shape sensitivity for every boundary point of the mesh will be implemented to get shape sensitivity for whole geometry.
- Further complex shape and mesh generation frameworks will be implemented using FreeCAD.

References

- [1] Matthew P. Juniper and R.I. Sujith. “Sensitivity and Nonlinearity of Thermoacoustic Oscillations”. In: *Annual Review of Fluid Mechanics* 50.1 (2018), pp. 661–689 (cit. on p. 1).
- [2] John William Strutt. *The Theory of Sound*. Vol. 1. Cambridge Library Collection - Physical Sciences. Cambridge: Cambridge University Press, 2011. ISBN: 978-1-108-03220-9 (cit. on p. 2).
- [3] Charles E. Martin et al. “Large-Eddy Simulation and Acoustic Analysis of a Swirled Staged Turbulent Combustor”. In: *AIAA Journal* 44.4 (Apr. 2006), pp. 741–750. ISSN: 0001-1452, 1533-385X (cit. on pp. 2, 12).
- [4] Pierre Wolf et al. “Acoustic and Large Eddy Simulation Studies of Azimuthal Modes in Annular Combustion Chambers”. In: *Combustion and Flame* 159.11 (Nov. 1, 2012), pp. 3398–3413. ISSN: 0010-2180 (cit. on pp. 2, 11).
- [5] T. Poinso. “Prediction and Control of Combustion Instabilities in Real Engines”. In: *Proceedings of the Combustion Institute* 36.1 (Jan. 1, 2017), pp. 1–28. ISSN: 1540-7489 (cit. on pp. 3, 11).
- [6] F. Nicoud et al. “Acoustic Modes in Combustors with Complex Impedances and Multidimensional Active Flames”. In: *AIAA Journal* 45.2 (Feb. 1, 2007), pp. 426–441. ISSN: 0001-1452 (cit. on pp. 3, 7, 8, 17).
- [7] Matthew P. Juniper. “Sensitivity Analysis of Thermoacoustic Instability with Adjoint Helmholtz Solvers”. In: *Physical Review Fluids* 3.11 (Nov. 21, 2018), p. 110509 (cit. on pp. 3, 11, 13, 21, 31, 32, 65).
- [8] D. Laera, G. Campa, and S. M. Camporeale. “A Finite Element Method for a Weakly Nonlinear Dynamic Analysis and Bifurcation Tracking of Thermo-Acoustic Instability in Longitudinal and Annular Combustors”. In: *Applied Energy* 187 (Feb. 1, 2017), pp. 216–227. ISSN: 0306-2619 (cit. on pp. 3, 39).
- [9] Xiaofeng Sun and Xiaoyu Wang. “Chapter 7 - Thermoacoustic Instability”. In: *Fundamentals of Aeroacoustics with Applications to Aeropropulsion Systems*. Ed. by Xiaofeng Sun and Xiaoyu Wang. Shanghai Jiao Tong University Press Aerospace Series. Oxford: Academic Press, Jan. 1, 2021, pp. 415–499. ISBN: 978-0-12-408069-0 (cit. on p. 3).
- [10] Ann P. Dowling and Simon R. Stow. “Acoustic Analysis of Gas Turbine Combustors”. In: *Journal of Propulsion and Power* 19.5 (Sept. 2003), pp. 751–764. ISSN: 0748-4658, 1533-3876 (cit. on p. 4).

- [11] Davide Laera et al. “Flame Describing Function Analysis of Spinning and Standing Modes in an Annular Combustor and Comparison with Experiments”. In: *Combustion and Flame* 184 (Oct. 2017), pp. 136–152. ISSN: 00102180 (cit. on pp. 4, 39, 41).
- [12] Nicholas A. Worth and James R. Dawson. “Self-Excited Circumferential Instabilities in a Model Annular Gas Turbine Combustor: Global Flame Dynamics”. In: *Proceedings of the Combustion Institute* 34.2 (Jan. 1, 2013), pp. 3127–3134. ISSN: 1540-7489 (cit. on p. 4).
- [13] Maria A. Heckl. “Active Control of the Noise from a Rijke Tube”. In: *Journal of Sound and Vibration* 124.1 (July 8, 1988), pp. 117–133. ISSN: 0022-460X (cit. on p. 4).
- [14] Ann P. Dowling and Aimee S. Morgans. “Feedback Control of Combustion Oscillations”. In: *Annual Review of Fluid Mechanics* 37.1 (2005), pp. 151–182 (cit. on p. 5).
- [15] Guangyu Zhang et al. “Control of Thermoacoustic Instability with a Drum-like Silencer”. In: *Journal of Sound and Vibration* 406 (Oct. 13, 2017), pp. 253–276. ISSN: 0022-460X (cit. on p. 5).
- [16] Dan Zhao et al. “Mitigation of Premixed Flame-Sustained Thermoacoustic Oscillations Using an Electrical Heater”. In: *International Journal of Heat and Mass Transfer* 86 (July 1, 2015), pp. 309–318. ISSN: 0017-9310 (cit. on p. 5).
- [17] Stefano Falco and Matthew P. Juniper. “Shape Optimization of Thermoacoustic Systems Using a Two-Dimensional Adjoint Helmholtz Solver”. In: *Journal of Engineering for Gas Turbines and Power* 143.7 (Mar. 31, 2021). ISSN: 0742-4795 (cit. on pp. 5, 36, 38, 40).
- [18] Antonio Andreini et al. “Assessment of Flame Transfer Function Formulations for the Thermoacoustic Analysis of Lean Burn Aero-Engine Combustors”. In: *Energy Procedia*. ATI 2013 - 68th Conference of the Italian Thermal Machines Engineering Association 45 (Jan. 1, 2014), pp. 1422–1431. ISSN: 1876-6102 (cit. on p. 11).
- [19] Luigi Crocco, Jerry Grey, and David T. Harrje. “Theory of Liquid Propellant Rocket Combustion Instability and Its Experimental Verification”. In: *ARS Journal* 30.2 (Feb. 1, 1960), pp. 159–168 (cit. on p. 11).
- [20] Perry Johnson. “Thermoacoustic Riemann Solver Finite Volume Method With Application To Turbulent Premixed Gas Turbine Combustion Instability”. In: (), p. 379 (cit. on p. 12).
- [21] Vicente Hernandez, Jose E. Roman, and Vicente Vidal. “SLEPc: A Scalable and Flexible Toolkit for the Solution of Eigenvalue Problems”. In: *ACM Transactions on Mathematical Software* 31.3 (Sept. 1, 2005), pp. 351–362. ISSN: 0098-3500 (cit. on pp. 17, 18).
- [22] Shrirang Abhyankar et al. *PETSc/TS: A Modern Scalable ODE/DAE Solver Library*. June 4, 2018. arXiv: 1806.01437 [math]. URL: <http://arxiv.org/abs/1806.01437> (visited on 11/02/2021) (cit. on p. 18).
- [23] Christophe Geuzaine and Jean-François Remacle. “Gmsh: A 3-D Finite Element Mesh Generator with Built-in Pre- and Post-Processing Facilities”. In: *International Journal for Numerical Methods in Engineering* 79.11 (2009), pp. 1309–1331. ISSN: 1097-0207 (cit. on p. 18).

-
- [24] James Ahrens, Berk Geveci, and Charles Law. “ParaView: An End-User Tool for Large-Data Visualization”. In: *Visualization Handbook*. Elsevier, 2005, pp. 717–731. ISBN: 978-0-12-387582-2 (cit. on p. 18).
 - [25] Stefano Falco. “Shape Sensitivity of Thermoacoustic Oscillations”. PhD thesis. University of Cambridge, 2021 (cit. on pp. 24, 34).
 - [26] Stephan Schmidt and Volker Schulz. “Shape Derivatives for General Objective Functions and the Incompressible Navier-Stokes Equations”. In: *Control and Cybernetics* 39.3 (2010), pp. 677–713. ISSN: 0324-8569 (cit. on p. 24).
 - [27] Jonathan P. Epperlein, Bassam Bamieh, and Karl J. Astrom. “Thermoacoustics and the Rijke Tube: Experiments, Identification, and Modeling”. In: *IEEE Control Systems Magazine* 35.2 (Apr. 2015), pp. 57–77. ISSN: 1941-000X (cit. on p. 31).
 - [28] Stefano Falco. “Shape Sensitivity of Thermoacoustic Instability”. First Year Report. University of Cambridge, 2021 (cit. on p. 33).
 - [29] Georg Atta Mensah. “Efficient Computation of Thermoacoustic Modes”. In: (2019) (cit. on pp. 39, 40).
 - [30] Brad Falck, Daniel Falck, and Brad Collette. *FreeCAD*. Packt Publishing Ltd, Sept. 18, 2012. 101 pp. ISBN: 978-1-84951-887-1. Google Books: yYITdzwValkC (cit. on p. 50).
 - [31] Martin Alnæs et al. “The FEniCS Project Version 1.5”. In: *Archive of Numerical Software* 3.100 (100 Dec. 7, 2015). ISSN: 2197-8263 (cit. on p. 55).
 - [32] *FEniCS/Dolfinx Repository*. GitHub. URL: <https://github.com/FEniCS/dolfinx> (visited on 11/02/2021) (cit. on p. 55).
 - [33] Les Piegl and Wayne Tiller. *The NURBS Book*. Springer Science & Business Media, Nov. 14, 1996. 664 pp. ISBN: 978-3-540-61545-3. Google Books: 7dqY5dyAwWkC (cit. on p. 67).

Appendix A

Thermoacoustic Eigensolver

Geometry files including Rijke tube and Micca combustor and implemented solver can be accessed by following GitHub repository;

- <https://github.com/ekremekc/Helmholtz-x>

Appendix B

Nondimensionalization

Nondimensionalization of the governing equations follows the same procedure in [7]. The characteristic length of the combustion chamber L_c , the ambient pressure p_a and the local speed of sound $c = \sqrt{\gamma p_a / \rho_a}$ are used during nondimensionalization process. If the quantities with ($\tilde{\cdot}$) denoted as nondimensional, the parameters of the problem can be seen in Table B.1;

Table B.1 Nondimensionalization of Quantities

Quantity	\mathbf{x}	t	ρ	\mathbf{u}	p
Nondimensionalized Quantity	$\tilde{\mathbf{x}}L_c$	$\frac{L_c \tilde{t}}{c}$	$\frac{\tilde{\rho} p_a}{\gamma}$	$\tilde{\mathbf{u}}c$	$\tilde{p} p_a$

Considering (2.23), the interaction index and time delay are rewritten as $n = \tilde{n} p_a L_c^2$ and $\tau = \tilde{\tau} L_c / c$, respectively.

All the nondimensional parameters in Table B.1 are inserted into (2.16). The obtained nondimensional equation stays same, apart from the parameter n . Since the interaction index is depending on the geometrical dimension of the analysis, the values are tabulated in Table B.2.

Table B.2 Nondimensionalization of parameter n

Dimension	Nondimensionalization relation
1D	$n_{dim} = \frac{n_{dim}}{(\pi/4)D^2}$
2D	$n_{dim} = \frac{n_{dim}}{(\pi/4)D}$
2D-Axisymmetric	$n_{dim} = \frac{n_{dim}}{(\pi/4)D}$
3D	$n_{dim} = n_{dim}$

In Table B.2, the subscript dim denotes dimensional quantity of interaction index and D is the radius of the tube. These relations come out due to the volume scaling of volumetric heat distribution function $v(\mathbf{x})$, introduced in §2.2.

Appendix C

BSpline Curves

To parametrize the boundaries which are considered to be optimized against thermoacoustic instability, BSpline curves are exploited due to their proven robustness for shape optimization problems. The reference is The NURBS Book[33].

BSplines require knot vector (\mathbf{u}), control points (\mathbf{X}) and degree (p) as an input parameters. Parametrized curve (\mathbf{K}) is calculated via basis functions ($N_{i,p}$). The i th BSpline basis function of order p reads;

$$N_{i,0}(u) = \begin{cases} 1, & \text{if } u_i \leq u < u_{i+1} \\ 0, & \text{otherwise} \end{cases} \quad (\text{C.1})$$

$$N_{i,p}(u) = \frac{u - u_i}{u_{i+p} - u_i} N_{i,p-1}(u) + \frac{u_{i+p+1} - u}{u_{i+p+1} - u_{i+1}} N_{i+1,p-1}(u) \quad (\text{C.2})$$

$$\mathbf{K}(u) = \sum_{i=0}^n N_{i,p}(u) \mathbf{X}_i \quad (\text{C.3})$$

C.1 Simple Example

Let's say we have knotvector as python numpy array and control points (x-y pairs) by following;

$$\begin{aligned} \mathbf{u} &= [0., 0.05, 0.1, 0.15, 0.2, 0.25, 0.3, 0.35, 0.4, 0.45, 0.5, \\ &\quad 0.55, 0.6, 0.65, 0.7, 0.75, 0.8, 0.85, 0.9, 0.95, 1.] \\ \mathbf{X} &= [(-1, 0), (1, 2), (1.5, 1.5), (3, 0)] \end{aligned}$$

By equations (C.1) and (C.2) the calculated basis functions with polynomial order 3 are shown in following Figure;

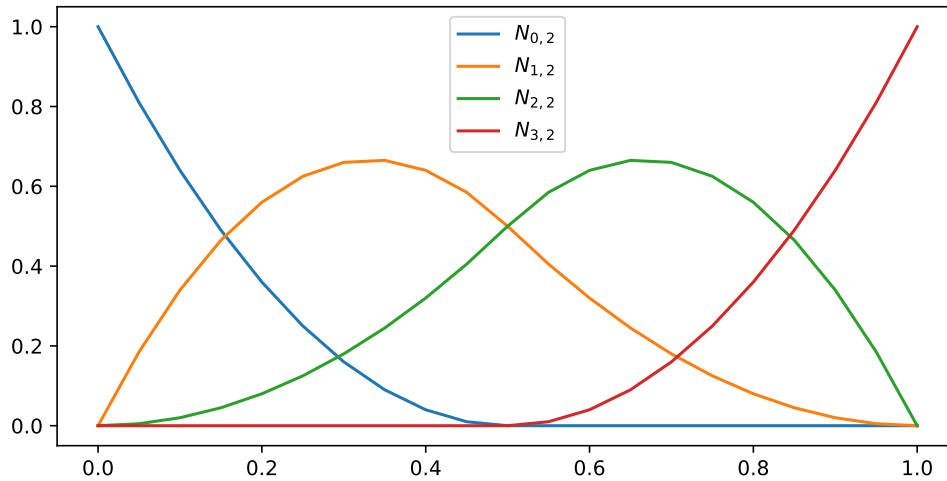
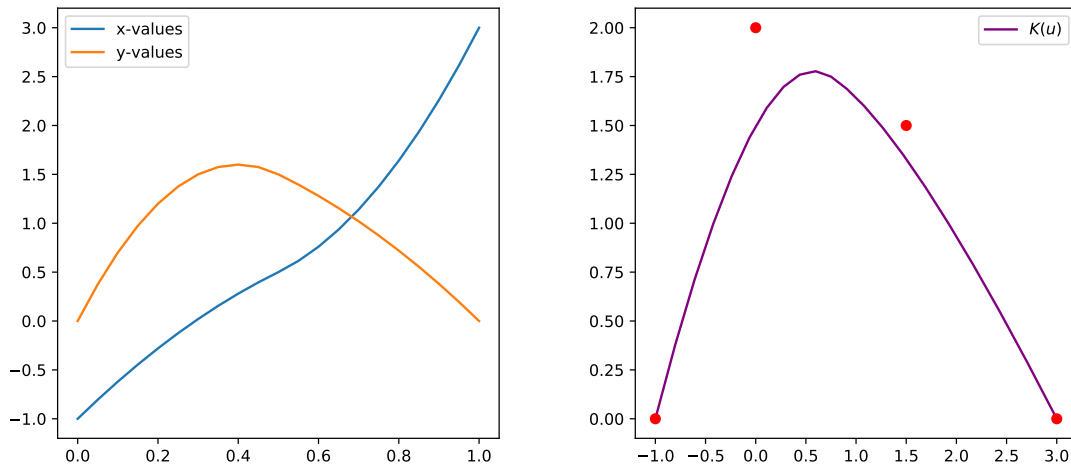


Fig. C.1 Basis functions for BSpline curve

And corresponding xy couples and curve shown in Figure C.2.



(a) Individual x and y values of curve

(b) BSpline curve

Fig. C.2 BSpline curve and its xy points

In Figure C.2b, it is clear to see that location of control points (red dots) effects the characteristic of the BSpline curve.